Earth-Science Reviews 248 (2024) 104647

Contents lists available at ScienceDirect

Earth-Science Reviews

journal homepage: www.elsevier.com/locate/earscirev

Invited Review

Spatiotemporal distribution of global mercury enrichments through the Paleocene-Eocene Thermal Maximum and links to volcanism

Simin Jin [a,b], David B. Kemp [a,*], Jun Shen [c], Runsheng Yin [d], David W. Jolley [e], Manuel Vieira [f], Chunju Huang [a,*]

[a] State Key Laboratory of Biogeology and Environmental Geology and Hubei Key Laboratory of Critical Zone Evolution, School of Earth Sciences, China University of Geosciences, Wuhan 430074, China
[b] Department of Atmospheric Science, School of Environmental Studies, China University of Geosciences, Wuhan 430074, China
[c] State Key Laboratory of Geological Processes and Mineral Resources, China University of Geosciences, Wuhan, Hubei 430074, PR China
[d] State Key Laboratory of Ore Deposit Geochemistry, Institute of Geochemistry, Chinese Academy of Sciences, Guiyang 550081, China
[e] Department of Geology & Geophysics, School of Geosciences, University of Aberdeen, King's College, Aberdeen AB24 3UE, UK
[f] GEOBIOTEC, Department of Earth Sciences, NOVA School of Science and Technology, Campus de Caparica, P-2829 516 Caparica, Portugal

ARTICLE INFO

Keywords:
PETM
North Atlantic Igneous Province
Mercury
Volcanism

ABSTRACT

Mercury (Hg) concentrations and Hg isotopes have been widely used to fingerprint geological volcanism. Mercury content, as a more accessible proxy, is more frequently used than mercury isotopes. With the deepening of research, however, it has been found that the Hg content of sediments can be strongly heterogeneous. The Paleocene–Eocene Thermal Maximum (PETM) was likely at least in part driven by magmatic activity based on multiple proxies, but existing PETM Hg records can be complex and sometimes ambiguous. To gain a global overview of the temporal and spatial distribution of Hg enrichment during the PETM, a compilation of new and existing mercury and associated data across this event from 19 globally distributed sites has been analyzed. Our findings indicate intercontinental Hg enrichment in the late Paleocene (~120 kyr prior to the PETM). Hg further increased ~30 kyr before, and within the onset of, the PETM carbon isotope excursion (CIE), supporting significantly increased volcanic Hg release and/or thermogenic Hg release via hydrothermal vent complexes (HTVCs) as the key trigger of the PETM. Evidence for magmatic activity during the CIE body is more complex and equivocal, and there is a general decline in Hg enrichment in the latter part of CIE body. This decline may indicate a decrease in volcanism, in-line with the general lack of tephra deposits close to the NAIP, and implies a decrease in highly explosive events capable of dispersing ash (and Hg) significant distances. Toward the end of and after the CIE, abundant tephras in the area proximal to the NAIP are contemporaneous with low Hg, suggesting a likely change in magmatic style and Hg flux, and emphasizing complexity in the expression of magmatism in sedimentary Hg data.

1. Introduction

The Paleocene–Eocene Thermal Maximum (PETM, ~56 Ma) was the most severe hyperthermal event of the Cenozoic. A large amount of carbon was released into the biosphere during the event. The source of the carbon is debated, but is thought to have been largely related to magmatism, and emitted from volcanoes (Jin et al., 2023; Gutjahr et al., 2017) and/or by thermogenic degassing from contact metamorphism via HTVCs (Frieling et al., 2016; Svensen et al., 2004, 2010). Other possible sources include methane hydrates and permafrost (Dickens et al., 1995; McInerney and Wing, 2011; DeConto et al., 2012). In recent years, a clear temporal coincidence between the PETM and emplacement of the North Atlantic Igneous Province (NAIP) has been established (Svensen et al., 2004, 2010; Frieling et al., 2016; Gutjahr et al., 2017; Jones et al., 2019; Stokke et al., 2020; Tremblin et al., 2022; Jin et al., 2023; Jones et al., 2023).

The NAIP initiated in the early Paleocene in the Rockall and Faroe-Shetland basins (Jolley et al., 2021 and references therein). From 62 Ma to 58.7 Ma, magmatism was mainly extrusive continental flood basalts (Wilkinson et al., 2017; Jolley et al., 2021). After a pause in magmatism at c. 57 Ma, voluminous extrusive volcanism occurred from c. 57–54 Ma (Saunders et al., 1997; Wilkinson et al., 2017; Jolley et al.,

* Corresponding authors.
E-mail addresses: davidkemp@cug.edu.cn (D.B. Kemp), huangcj@cug.edu.cn (C. Huang).

https://doi.org/10.1016/j.earscirev.2023.104647
Received 10 June 2023; Received in revised form 24 November 2023; Accepted 1 December 2023
Available online 7 December 2023

2021). Average melt production rate increased by an order of magnitude at 56.1 ± 0.5 Ma (Storey et al., 2007), broadly coincident with the PETM.

The role of the NAIP in triggering and sustaining the PETM has been explored in recent years using volcanism proxies such as Os isotopes, sedimentary Hg enrichment and Hg isotopes, as well as modeling (Schmitz et al., 2004; Svensen et al., 2004, 2010; Wieczorek et al., 2013; Dickson et al., 2015; Frieling et al., 2016; Gutjahr et al., 2017; Jones et al., 2019, 2023; Liu et al., 2019; Jin et al., 2023). Sedimentary Hg abundance, as the most accessible of these proxies, provides a chance to explore the impact of NAIP magmatic activity on the global environment during the PETM from a wide range of sedimentary environments and localities.

The utility of sedimentary Hg as a volcanism proxy is predicated on the inference that volcanic emission was the dominant source of Hg in the surface environment during preindustrial periods (Pyle and Mather, 2003; Selin, 2009). The residence time of gaseous Hg^0 emitted from volcanoes is ~0.5–1 years, which allows Hg to disperse potentially globally prior to its deposition (Schroeder and Munthe, 1998; Selin et al., 2008). Sedimentary Hg enrichment that cannot be readily explained via changes in the abundance of minerals and sedimentary components that typically host Hg (e.g., organic matter and sulfide minerals, Shen et al., 2020) can thus provide a fingerprint of volcanism.

There are two potential Hg sources associated with NAIP activity (Jones et al., 2023, see also Jin et al., 2023). The first is volcanic Hg emitted during either subaerial or submarine eruptions. The increased melt production rate (Storey et al., 2007), and the presence of numerous ash layers derived from the NAIP in northern Europe during the PETM provide support for volatile volcanic Hg emitted during explosive and effusive subaerial eruptions (Bøggild, 1918; Jones et al., 2019). A second source of Hg is sedimentary Hg found in organic-rich rocks that is thermogenically volatilized by contact metamorphism and released through HTVCs (Svensen et al., 2004, 2010, 2023). Support for thermogenic release of Hg via HTVCs at the PETM comes from the observation that vent complexes in the NAIP formed just before and during the PETM (Frieling et al., 2016; Berndt et al., 2023).

Unlike the globally distributed (or at least universally observed) Hg enrichment in sedimentary strata spanning the end-Permian extinction (252 Ma, Shen et al., 2019a, 2023), the distribution of Hg enrichment during the PETM demonstrates significant spatial heterogeneity. Hg enrichment has been recorded within, or just prior to the PETM, indicating a temporal link between the onset of the event and volcanism (e.g. sites in the North Sea Basin close to the NAIP and Spain; Jones et al., 2019; Kender et al., 2021; Tremblin et al., 2022). Equally, however, for sections deposited >2500 km away from the NAIP, Hg enrichment may not be pronounced, such as New Jersey coastal plain sites (Liu et al., 2019; Jones et al., 2019).

To date, the global spatiotemporal pattern of Hg enrichment through the PETM remains unclear. To better understand the variations in intensity and magnitude of volcanism, we compile and review the evidence for Hg enrichment changes across the PETM globally, and present new Hg abundance data from five globally distributed sites. Our new analysis provides: 1) a composite record of Hg enrichment versus age across the PETM, and 2) a holistic picture of the global distribution of Hg during the PETM and the geological/regional factors that affected the abundance of Hg in sedimentary rocks.

2. Background

Once emitted, most Hg will be dispersed into the atmosphere in the form of gaseous Hg^0, whereas the remainder will be deposited locally as oxidized or particulate species (Bagnato et al., 2007). One fraction of the gaseous Hg^0 in the atmosphere can be taken up directly by plant foliage and buried in soil and thus hosted by organic matter (OM), whilst another fraction of the Hg^0 will be oxidized to reactive Hg^{2+} and deposited on land/water via precipitation (wet deposition). A small fraction of Hg^0 will be attached to aerosols and deposited directly via dry deposition (Schroeder and Munthe, 1998; Selin, 2009; Demers et al., 2013). In sulfidic environments, Hg-sulfide complexes are the dominant scavengers of Hg due to the higher stability constants compared to Hg-organic complexes (Ravichandran, 2004; Shen et al., 2019b, 2020). In relatively low organic matter and/or oxidizing environments (e.g., coastal oceans), clay minerals (especially smectite) can also scavenge Hg from the water column owing to the relatively high surface area reactivity, moderate to high cation exchange capacity, and high negative surface charge (Farrah and Pickering, 1978; Horowitz, 1991; Kongchum et al., 2011; Shen et al., 2020). The mercury adsorption ability of clay is an order of magnitude higher than quartz and feldspar (Tessier et al., 1982).

To quantify Hg enrichment in sediments and rocks, it is important to diagnose the dominant host of Hg first and then normalize correctly (by calculating the Hg/host phase ratio) (Shen et al., 2019b). The normalization process for mercury can also introduce errors. For example, lithological variations between samples within the same section/environment could correspond to changes in host phase. Even with the correct host phase identified, normalization of Hg can still be affected by the analytical precision of the host index data. For example, if normalizing to organic matter (i.e., total organic carbon: TOC), Grasby et al. (2016) suggest that only Hg/TOC ratios from samples with TOC >0.2% should be considered reliable, since this is close to the analytical precision of most pyrolysis-based TOC measurements, and at very low concentrations small errors in TOC will lead to significant changes in Hg/TOC.

The abundance of Hg in sediments and sedimentary rocks is controlled by two factors: the flux of Hg, e.g., from terrestrial input or volcanism, and the preservation of Hg. Mercury preservation is affected by the local depositional environment (e.g., redox state, Shen et al., 2019b, 2020; Frieling et al., 2023), and post-depositional processes (e.g., diagenesis and weathering, Charbonnier et al., 2020; Park et al., 2022).

During post-depositional oxidization/weathering, the disproportionate loss of organic matter and sulfide minerals relative to Hg can lead to anomalous Hg enrichment signals (Charbonnier et al., 2020; Park et al., 2022). With clay-hosted Hg, smectite has relatively higher Hg scavenging ability (Kongchum et al., 2011) and weathering may affect Hg content through the transformation of clay minerals (i.e., the disproportionate loss of smectite). In environments with low-oxygen, underestimation of Hg/TOC can come from: 1) the transformation of stable organic matter-bound mercury into more active forms under ferruginous to (mildly) euxinic conditions, such as iron and manganese oxyhydroxides, which facilitate the evasion of Hg from sediments (Frieling et al., 2023); 2) enhanced burial efficiency of TOC under low-oxygen conditions whilst Hg concentrations remain broadly stable (Emili et al., 2011; Frieling et al., 2023).

Assuming these non-volcanic factors can be recognized and appropriately dealt with, Hg concentrations in sedimentary rocks remain a powerful fingerprint of volcanism. Even so, the actual type of volcanism can vary greatly. It can be submarine or continental, involve intrusion into organic-rich rocks, and can have varying explosivity. All of these factors can fundamentally impact the flux and dispersion of Hg in ways that are not well understood. For instance, Hg emissions from submarine volcanic activity are expected to have a limited dispersal range, whilst those resulting from explosive volcanism with high altitude dispersal of gases and ashes are more likely to be globally distributed (Scaife et al., 2017; Percival et al., 2018). In addition, thermogenic Hg emissions from HTVCs are variable, and may contain very high levels of Hg but with a limited dispersal range (<20 km, Tomiyasu et al., 2007; Jones et al., 2019; Berndt et al., 2023; Svensen et al., 2023). As noted in Section 1, two Hg sources were likely involved during the PETM: volcanic fluxes from explosive and effusive sources, and thermogenic sources from HTVCs. In addition to differences in dispersal range of these two Hg sources, there are also differences in the isotopic composition of Hg.

Svensen et al. (2023) show that Hg released via HTVCs yielded a mixed magmatic-sedimentary isotopic signature (i.e., negative Hg isotope mass-independent fractionation values).

3. Materials and methods

3.1. Data compilation

We compiled Hg abundance data and associated compositional data from 19 PETM sites worldwide (Fig. 1, Table 1). Carbon isotope data from each site allow for the definition of the PETM and its constituent phases (i.e., onset, body and recovery) based on the presence of the ubiquitous negative carbon isotope excursion (CIE) that marks the PETM. Sites are correlated using the CIEs recorded at each site, and the sedimentary successions of each site are subdivided into pre-CIE, CIE onset, CIE body, CIE recovery and post-CIE intervals (see Supplementary Data for the division of each site; Fig. 7). The age model used for the CIE at all sites is based on the 200 kyr duration estimated by Westerhold et al. (2018); with a CIE onset of 20 kyr, CIE body of 100 kyr, and CIE recovery of 80 kyr (Westerhold et al., 2018; see also Cui et al., 2011). The sedimentation rate of strata above and below the CIE at each site is assumed to be equal to the mean sedimentation rate within the CIE.

Fourteen of the sites are from previously published research (Table 1). The North Sea Basin wells 25/11–17, 22/10a-4, 23/16b-9 and E-8X are characterized by claystone and sandstone. For Well 22/10a-4, only claystone samples were analyzed from pre-CIE to the lower part of the CIE body (Kender et al., 2021). The Fur Island section in northern Denmark is characterized by marine clays and interbedded ash layers (Jones et al., 2019). Core BH09/2005 from the eastern margin of the Central Basin of Spitsbergen consists of mudstones (Jones et al., 2019). Sections from the Pyrenees include the marine sections of Zumaia and Lussagnet (characterized by limestone with siliciclastic inputs), and the continental sections of Esplugafreda and Serraduy (dominated by silty shale) (Tremblin et al., 2022). On the New Jersey coastal plain, cores through the Bass River and Millville show lithological variation during the PETM, with glauconite-rich siltstone above and below, but clay-dominated sedimentary rocks during the PETM. A shift toward finer sedimentary rocks during the PETM is observed in the Millville core (Jones et al., 2019; Liu et al., 2019). The PETM sediments at the Blake Nose core in the North Atlantic consist of carbonate-rich pelagic sediments (Liu et al., 2019). The Global Stratotype Section and Point at the Dababiya quarry section in Egypt are composed of marls and non-calcareous clays (Keller et al., 2018).

Data from the other five sites are from this study (Fig. 1). These are: Well 30/14–1 in the North Sea Basin, 2 cores (Wilson Lake and Ancora) from the New Jersey Ocean Drilling Program (ODP) Leg 174AX, ODP Site 1262 in the South Atlantic deep-sea, and Hole 4 A from the International Ocean Discovery Program (IODP) Arctic Coring Expedition (ACEX) (Jones et al., 2019).

Well 30/14–1 (56°33′37″N, 2°38′08″E) is located in the central North Sea Basin. The lithology at 30/14–1 is characterized by claystone (Fig. 2). The PETM was previously identified in this well from a core depth of 2927 m to 2903 m based on both a > 2‰ negative CIE and the presence of the dinoflagellate *Apectodinium*, which has an acme during the PETM (Fig. 2; Sluijs et al., 2007). For this study, 56 samples were collected every ~1 m across the PETM (2880.15 m to 2940.16 m). Samples were measured for organic carbon isotopes ($\delta^{13}C_{org}$), Hg, TOC, total sulfur (TS), total nitrogen (TN) and major element abundances.

The ACEX core site (87°52′12″N, 136°12′41″E) is located on the Lomonosov ridge in the central Arctic Ocean. The sedimentary rocks are characterized by organic-rich siliciclastic claystone. The PETM was identified from ~387 to 378.5 m, albeit with disturbance by drilling that interrupts the interval between 388.5 and 388 m composite depth, and loss of the CIE onset due to coring gaps between 388 and 384.25 m (Fig. 3; Sluijs et al., 2006). Jones et al. (2019) previously published Hg abundance and Hg/TOC data from this site. Here, a further 56 samples from the ACEX core were obtained every ~0.2 m across the PETM CIE to increase the resolution of this previous work and extend the data into older and younger strata. All samples were measured for Hg, TOC, TS, TN and major element abundances.

The ODP Leg 174AX Wilson Lake and Ancora core sites are located on the New Jersey coastal plain on the American continental shelf ~17.5 km apart from each other (39°39′21″N, 75°02′52″W and 39°41′32″N, 74°50′56″W, respectively). Sedimentary rocks from these two cores are characterized by fine to medium glauconite-rich sandstone below and above the PETM interval, and finer claystone during the PETM (Figs. 4 and 5; Stassen et al., 2012). For this study, 42 samples were collected every ~1 m from the Wilson Lake core and 41 samples

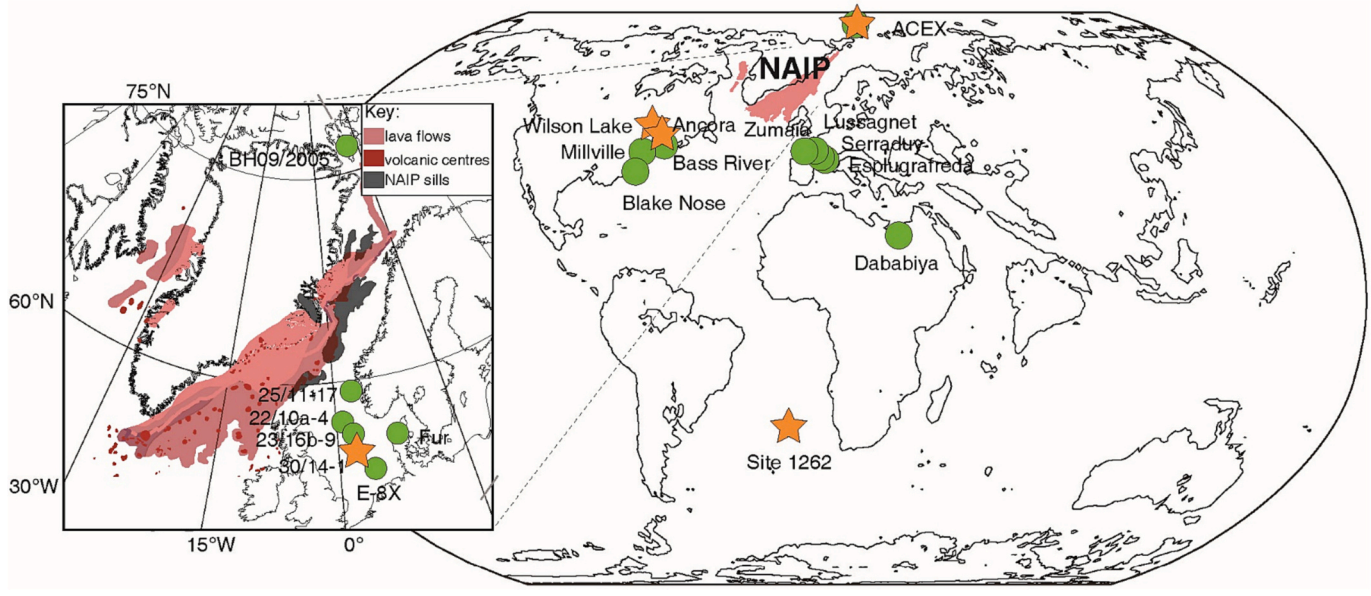

Fig. 1. Map showing the 19 studied PETM sites. Sites with new Hg and associated data presented in this study are marked with orange stars. These are: Well 30/14–1, ACEX, ODP Leg 174AX and ODP Site 1262. Sites with previously published Hg data are marked with green circles. See Table 1 for further details and references, and also Supplementary Data. Maps are modified from Jones et al. (2019) and Tierney et al. (2020). (For interpretation of the references to colour in this figure legend, the reader is referred to the web version of this article.)

Table 1
Full list of the studied PETM sites, ordered by distance from the NAIP (closer to further). Other information shown includes the Pearson r correlation coefficients (and *p*-values in brackets) between Hg and TOC, TS, Al, Mn and Fe. Based on these correlations, the likely dominant host phase of Hg is indicated. The confidence in this host phase assignment is based on the *p* values and amount of data. 'Not robust' indicates a lack of data and/or insignificant p values. The median value of TOC and Hg in each site is also provided. OM = organic matter.

Study site	Location	n	Paleo-environment	Pearson r values (significance in brackets)					Dominant host phase	median		reference
				Hg and TOC	Hg and TS	Hg and Al	Hg and Mn	Hg and Fe		median of TOC	median of Hg	
25/11–17	North Sea Basin	9	deep ocean basin	−0.33 (*0.21*)					OM (not robust)	1.37	4625.0	Jones et al., 2019
22/10a-4	North Sea Basin	139	deep ocean basin	**0.49** (*<0.001*)					OM (not robust)	1.27	77.0	Kender et al., 2021
23/16b-9	North Sea Basin	122	deep ocean basin	**0.34** (*<0.001*)	**0.57** (*<0.001*)	**−0.708** (*<0.001*)	**0.43** (*<0.001*)	**−0.35** (*<0.001*)	sulfide (robust)	1.23	97.3	Jin et al., 2023
30/14–1	North Sea Basin	56	deep ocean basin	0.13 (*0.36*)	0.08 (*0.57*)	0.18 (*0.19*)	0.08 (*0.58*)	**0.50** (*<0.001*)	Fe-ox (robust)	1.19	71.2	this study
Fur Island	North Sea Basin	112	shallow marine	**0.31** (*<0.001*)					OM (not robust)	1.08	41.8	Jones et al., 2019
E-8X	North Sea Basin	156	deep ocean basin	**0.63** (*<0.001*)					OM (not robust)	2.38	91.5	Kender et al., 2021
BH09/2005	Arctic	147	shallow marine	**0.25** (*<0.001*)					OM (not robust)	1.28	31.5	Jones et al., 2019
ACEX	Arctic	71	shallow marine	0.13 (*0.28*)	0.07 (*0.68*)	0.08 (*0.65*)	0.05 (*0.76*)	0.38 (*0.03*)	Fe-ox (not robust)	2.30	98.0	Jones et al., 2019, this study
Zumaia	Pyrenean foreland basins	80	deep ocean basin	−0.02 (*0.89*)		0.10 (*0.37*)	−0.04 (*0.74*)	0.06 (*0.60*)	OM (not robust)	0.09	17.3	Tremblin et al., 2022
Lussagnet	Pyrenean foreland basins	132	shallow marine	**0.79** (*<0.001*)			−0.05 (*0.65*)		OM (not robust)	0.06	19.7	Tremblin et al., 2022
Serraduy	Pyrenean foreland basins	38	continental	**0.60** (*<0.001*)					OM (not robust)	0.04	1.3	Tremblin et al., 2022
Esplugafreda	Pyrenean foreland basins	39	continental	**0.38** (*0.03*)					OM (not robust)	0.04	1.6	Tremblin et al., 2022
Ancora	US	41	shelf	−0.11 (*0.47*)	0.10 (*0.10*)	**0.85** (*<0.001*)	**0.36** (*0.02*)	0.17 (*0.30*)	clay (robust)	0.29	13.7	this study
Wilson Lake	US	42	shelf	**0.66** (*<0.001*)	**0.47** (*0.00*)	**0.82** (*<0.001*)	**0.45** (*0.003*)	−0.28 (*0.07*)	clay (robust)	0.30	14.8	this study
Bass River	US	49	shelf	−0.13 (*0.37*)					OM (not robust)	0.24	19.0	Jones et al., 2019
Millville	US	26	shelf	**0.93** (*<0.001*)					OM (not robust)	0.38	22.4	Liu et al., 2019
Blake nose	Atlantic	23	deep ocean	0.27 (*0.22*)					OM (not robust)	0.08	3.8	Liu et al., 2019
Dababiya	Egypt	54	shallow marine	**0.60** (*<0.001*)					OM (not robust)	0.30	85.3	Keller et al., 2018
1262	Atlantic	43	deep ocean	**0.40** (*0.003*)	**0.38** (*0.013*)	−0.19 (*0.494*)	**0.62** (*0.001*)	**0.33** (*0.031*)	Mn-ox (robust)	0.01	1.3	this study

were collected every ~0.2 m from the Ancora core. Samples were measured for Hg, TOC, TS, TN and major element abundances.

ODP Leg 208 Site 1262 is located on Walvis Ridge in the southern Atlantic Ocean (27°11′9″S, 1°34′37″E). The core is characterized by an abrupt transition from carbonate to claystone at the CIE onset, which marks a dissolution of sea-floor carbonate (Fig. 6; Zachos et al., 2005). Fifty samples were collected every ~0.02 m across the PETM from 159.92 m to 136.01 m composite depth. Samples were analyzed for Hg, TOC, TS, TN and major element abundances.

3.2. Geochemical methods

All 245 samples (56 for 30/14–1, 56 for IODP 302, 42 for Wilson Lake, 41 for Ancora and 50 for Site 1262) were crushed to ~200 mesh in an agate mortar before analysis. Powdered samples were divided into several parts for sample pretreatment. The Hg content of all samples was measured using a Milestone Direct Mercury Analyzer (DMA-80 Evo) at China University of Geosciences (Wuhan). Measurement of a soil standard reference material (GBW07423) yielded a relative standard deviation (RSD) of ±10% ($n = 24$) for Hg content.

For TOC, TS and TN analysis, an aliquot of each sample was reacted with 15 ml of 3 M HCl for 72 h to remove all carbonate, and then rinsed with deionized water until the supernatant was neutral. After freeze-drying and re-powdering, samples were analyzed using a Vario MACRO Cube elemental analyzer in the School of Materials Chemistry, China University of Geosciences (Wuhan). Precision of the TN, TOC and TS data, based on analyses of a Phenylalanine standard, was 0.08%, 0.22% and 0.18%, respectively (weight%, 2σ).

Fifty-six decalcified and dried samples from Well 30/14–1 were measured for bulk organic carbon isotopes ($\delta^{13}C_{org}$) using a Thermo Finnigan MAT 253 mass spectrometer. Analysis of laboratory standards yielded a reproducibility of ±0.09‰ (2σ). Analyses were conducted at School of Earth Sciences, China University of Geosciences (Wuhan).

Powdered aliquots of all samples were analyzed for major element abundances using an Olympus VCA (Vanta) handheld XRF analyzer following methods in Saker-Clark et al. (2019). Repeat measurements of samples yielded a precision of 0.19%, 0.13% and 140 ppm (2σ) for Al, Fe and Mn, respectively.

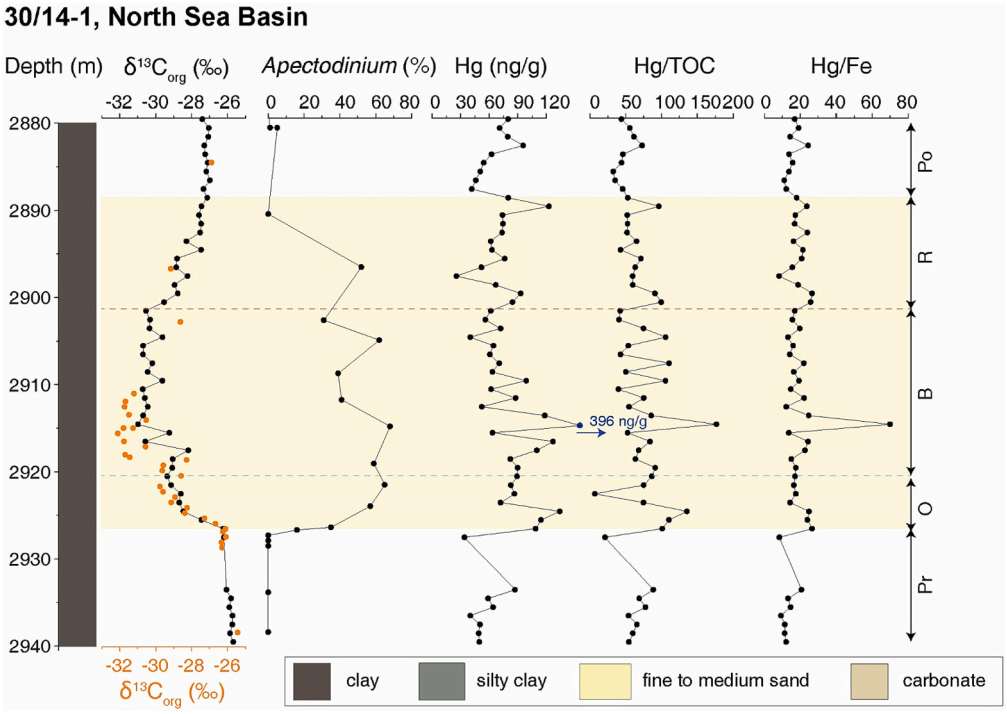

Fig. 2. Lithological and geochemical data from Well 30/14–1. Orange organic carbon isotope ($\delta^{13}C_{org}$) data and specimen percentage of *Apectodinium* data are from Sluijs et al. (2007). Black organic carbon isotope ($\delta^{13}C_{org}$), Hg, Hg/TOC and Hg/Fe data are from this study. PETM CIE is highlighted with yellow shading. Pr = pre-CIE, O = CIE onset, B = CIE body, R = CIE recovery, Po = post-CIE. (For interpretation of the references to colour in this figure legend, the reader is referred to the web version of this article.)

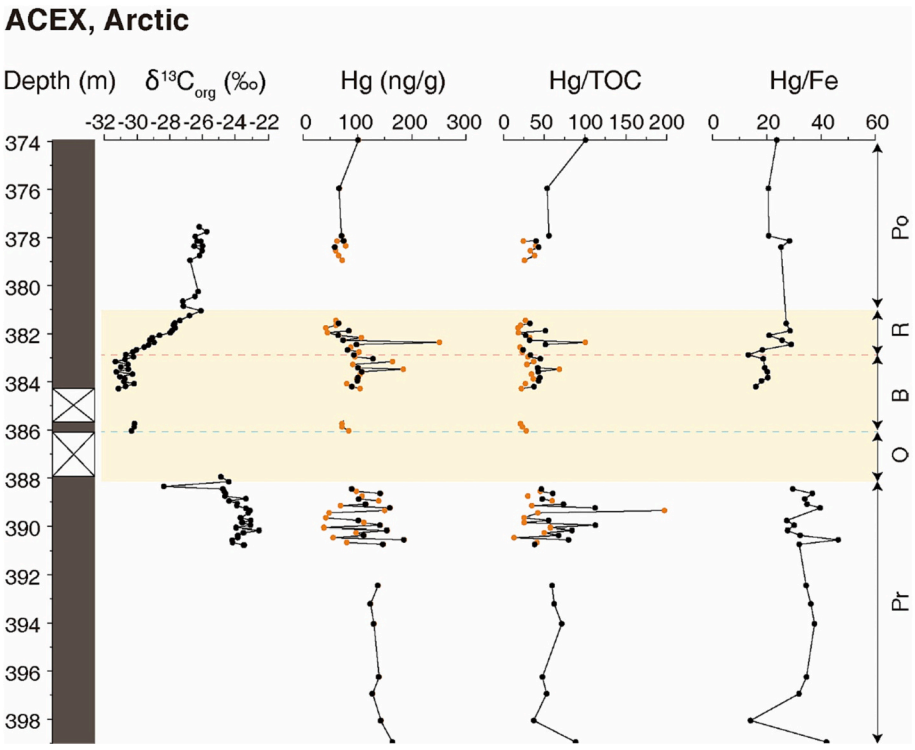

Fig. 3. Lithological and geochemical data in well ACEX. $\delta^{13}C_{org}$ data are from Sluijs et al. (2006). The orange data points of Hg and Hg/TOC are from Jones et al. (2019). Black data points of Hg, Hg/TOC and Hg/Fe are from this study. PETM CIE is highlighted with yellow shading. Pr = pre-CIE, O = CIE onset, B = CIE body, R = CIE recovery, Po = post-CIE. For interpretation of lithology, see key in Fig. 2. (For interpretation of the references to colour in this figure legend, the reader is referred to the web version of this article.)

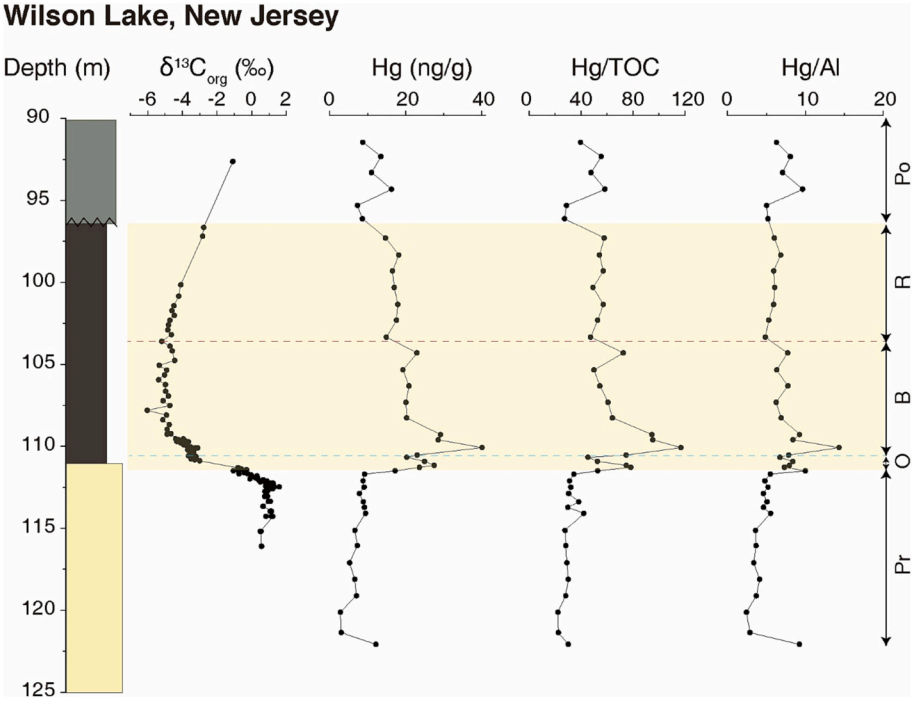

Fig. 4. Lithological and geochemical data in ODP Leg 174AX Wilson Lake. $\delta^{13}C_{org}$ data are from Wright and Schaller (2013). Hg, Hg/TOC and Hg/Al data are from this study. PETM CIE is highlighted with yellow shading. Pr = pre-CIE, O = CIE onset, B = CIE body, R = CIE recovery, Po = post-CIE. For interpretation of lithology, see key in Fig. 2. (For interpretation of the references to colour in this figure legend, the reader is referred to the web version of this article.)

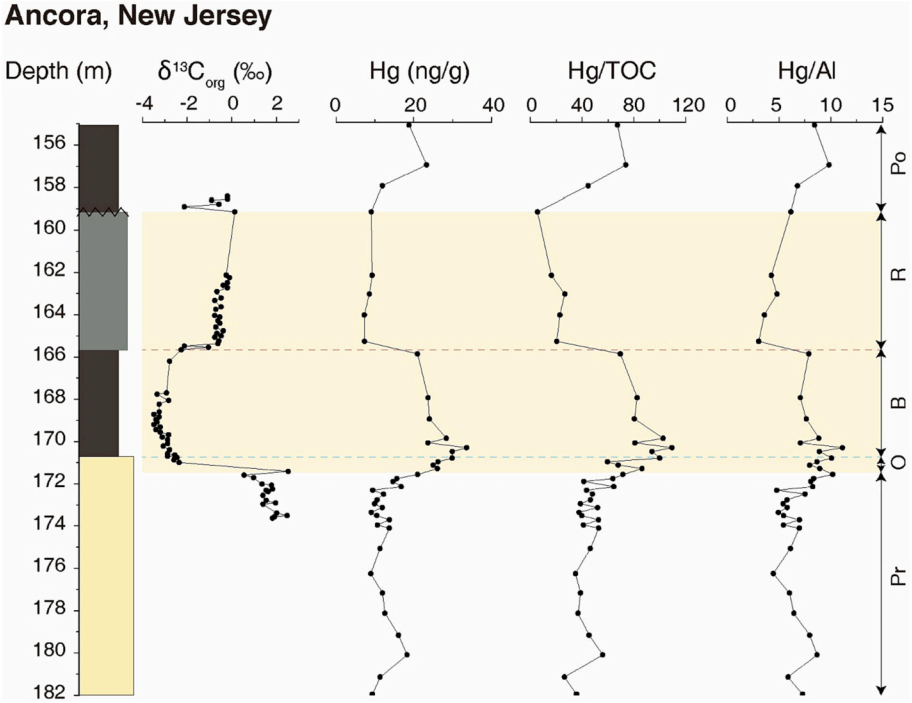

Fig. 5. Lithological and geochemical data in ODP Leg 174AX Ancora. $\delta^{13}C_{org}$ data are from Makarova et al. (2017). Hg, Hg/TOC and Hg/Al data are from this study. PETM CIE is highlighted with yellow shading. Pr = pre-CIE, O = CIE onset, B = CIE body, R = CIE recovery, Po = post-CIE. For interpretation of lithology, see key in Fig. 2. (For interpretation of the references to colour in this figure legend, the reader is referred to the web version of this article.)

3.3. Hg enrichment factors

Previous work has introduced the concept of using Hg enrichment factors (Hg_{EF}) to make comparisons between sites deposited in very different environments, with likely differing host phases (Shen et al., 2019c). Hg_{EF} is calculated as the ratio between the host-phase normalized Hg of the samples and some background (and non-volcanically influenced) value. For example, if organic matter is the primary host of Hg, then Hg_{EF} can be calculated via:

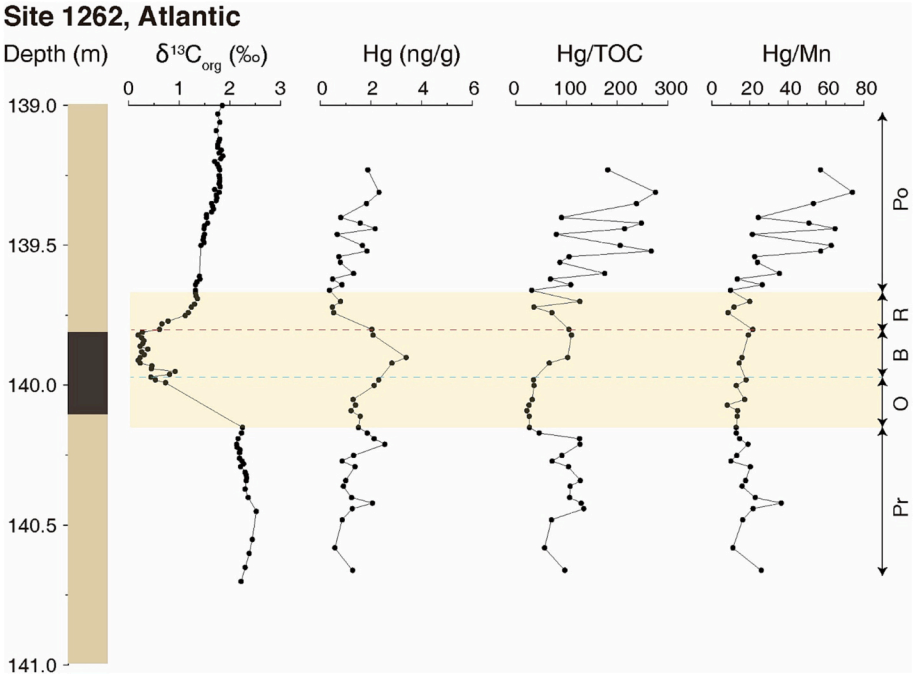

Fig. 6. Lithological and geochemical data in ODP Site 1262. $\delta^{13}C_{org}$ data are from Zachos et al. (2010). Hg, Hg/TOC and Hg/Mn data are from this study. PETM CIE is highlighted with yellow shading. Pr = pre-CIE, O = CIE onset, B = CIE body, R = CIE recovery, Po = post-CIE. For interpretation of lithology, see key in Fig. 2. (For interpretation of the references to colour in this figure legend, the reader is referred to the web version of this article.)

$$Hg_{EF} = (Hg/TOC)_{sample} \Big/ (Hg/TOC)_{background} \quad (1)$$

Where background refers to the mean value of Hg and host phase components in an average clastic sedimentary rock. Mean Hg and Hg/TOC were recently quantified as 62.4 ng/g, and 71.9, respectively (Grasby et al., 2019). Given the lack of widespread sulfidic environments during the PETM, the reported mean values of TS, Al, Mn and Fe are derived from the analysis of published mean values of non-sulfide-hosted Hg in sedimentary rocks from previous studies (Shen et al., 2020; Hu et al., 2021; Sial et al., 2021; Liu et al., 2021a; Liu et al., 2021b; Zan et al., 2021; Zhao et al., 2022a; Zhao et al., 2022b; Qiu et al., 2022; Wang et al., 2023; Wu et al., 2022; Liu et al., 2023; Shen et al., 2022a; Tang et al., 2022; Rakociński et al., 2022). The specific background mean values used are as follows: mean Hg/TS = 79.0, mean Hg/Al = 24.5, mean Hg/Mn = 687, mean Hg/Fe = 21.9. Although the use of these values represents a convenient and consistent way of calculating enrichment factors, the values used may be biased toward higher Hg contents, since the data come from published studies that intentionally focused on periods of environmental instability with perhaps higher Hg contents than normal background levels. Nevertheless, the key aim with the calculation of Hg enrichment factors in this study is to standardize data in such a way that trends in Hg_{EF} (rather than absolute values) can be readily assessed and compared. Thus, sedimentary systems with Hg contents and normalized Hg contents lower than these does not mean that they cannot be enriched in Hg.

4. Results

4.1. New Hg data

In Well 30/14–1, Hg content ranges from 25.5 to 396.0 ng/g (mean 78.9 ng/g). Hg abundance is relatively stable across the PETM CIE, with a single peak of 396.0 ng/g at 2915.17 m (Fig. 2). Hg abundance across the ACEX core is consistent with previous work (Fig. 3; Jones et al., 2019). Hg abundance is relatively high from 398.1 to 390.8 m before the CIE onset (mean 136 ng/g), and becomes more variable above 390.8 m, with peaks between 383.54 and 382.42 m toward the end of the CIE body and the early part of the CIE recovery (maximum 251 ng/g).

At Wilson Lake, Hg contents are relatively low and stable below 111.88 m before the CIE onset (mean 7.8 ng/g) and increase (maximum 40.1 ng/g) steadily up until 97.48 m within the CIE (mean 21.6 ng/g). After the CIE, the Hg content returns to pre-CIE values (10.88 ng/g; Fig. 4). At Ancora, Hg concentrations show a similar trend to Wilson Lake through the PETM (Fig. 5). Before the CIE Hg is relatively low, with a mean of 11.3 ng/g below 172.38 m. There is a trend toward higher values across the CIE onset from 172.38 to 170.37 m (maximum 33.6 ng/g). Hg content remains relatively high during the CIE body from 170.37 to 165.93 m, and then decreases back to pre-CIE values (mean 9.2 ng/g) (Fig. 5).

At Site 1262, Hg concentrations are very low, with an average of 1.4 ng/g. A trend in Hg through the PETM is discernable, with Hg values relatively high at the end of CIE onset and the upper part of the CIE body between 140.05 and 139.8 m (2.3 ng/g; Fig. 6). Above the CIE body, Hg values return to pre-CIE values, with a mean of 1.1 ng/g (Fig. 6).

5. Discussion

5.1. Sedimentary host phases of Hg

As discussed in Section 2, organic matter, sulfide, clay minerals, and iron and manganese oxyhydroxides can all act as hosts of sedimentary Hg (e.g., Boszke et al., 2003; Shen et al., 2020). The strength of correlation between Hg and TOC, TS, Al, Fe and Mn can be used to indicate the likely host of Hg, based on the assumption that the correlation with the highest Pearson r value is the dominant host phase (Shen et al., 2019d).

In Well 30/14–1, the host of Hg is considered to be iron oxyhydroxides based on the significant correlation between Hg and Fe (r = 0.50, n = 56, p-value <0.001), and lack of significant correlation with any other host phase (Table 1). At Ancora and Wilson Lake, the strong correlation between Hg and Al (a broad proxy for clay content), suggests that clays are the dominant host of Hg (r = 0.85, n = 41, p-value <0.001 and r = 0.82, n = 42, p-value <0.001 respectively, Table 1). At ODP Site

1262, Hg has a significant correlation with TOC, TS, Mn and Fe (r = 0.40, n = 43, p-value = 0.003; r = 0.38, n = 43, p-value = 0.013; r = 0.62, n = 43, p-value <0.001 and r = 0.33, n = 43, p-value = 0.031, respectively, Table 1). Indeed, there is strong correlation between all these proxies (e.g., r = 0.985, p-value <0.001; r = 0.740, p-value <0.001 and r = 0.973, p-value <0.001 between TOC and TS, TOC and Mn, and TOC and Fe, respectively), and Hg/TOC, Hg/TS, Hg/Fe and Hg/Mn all show similar profiles. These high correlations are likely the result of the strong dilution effect of carbonate in the section (which does not host Hg). Manganese oxyhydroxides may be the dominant host of Hg given the relatively higher Pearson r values. At ACEX, there is a significant correlation between Hg and Fe (r = 0.38, n = 35, p-value = 0.03) which suggests that iron oxyhydroxides may be the dominant host of Hg. As discussed in Jin et al. (2023), sulfide and organic matter are inferred to be the dominant hosts of Hg in Well 23/16b-9.

At other sites with only published Hg and TOC data, Hg and TOC show significant correlation at a majority of sites (e.g., 22/10a-4, Fur Island, E-8X, BH9–05, Lussagnet, Serraduy, Esplugafreda, Millville, Dababiya, Table 1). The weak and insignificant correlation between Hg and TOC in Well 25/11–17 (r = −0.33, p-value = 0.21) may be related to the extremely high concentration of Hg at this site (which could have been released from nearby submarine HTVCs, Jones et al., 2019). The negligible/weak correlations between Hg and TOC at Zumaia and Blake Nose (r = −0.02, p-value = 0.89 and r = 0.27, p-value = 0.22, respectively) may be related to the low TOC content close to or below the analytical precision of the TOC data. Notably, TOC varied from 0.0 to 0.3% at Zumaia, and the analytical precision (2σ) of these data was 0.1% (Tremblin et al., 2022).

Taken together, organic matter was likely the dominant host of Hg at most sites during the PETM (Table 1). Mercury and TOC show a power law relationship for all of the samples across the PETM in the studied sites ($Hg = 58*TOC^{0.72}$, n = 1032; using only TOC concentrations >0.2%). This relationship is similar with the relationship that Grasby et al. (2013) defined using Permian-Triassic samples ($Hg = 48.5*TOC^{0.89}$) and supports a strong link between Hg and organic matter in the sedimentary record. At the same time, however, non-organic matter hosting of Hg clearly occurs. Although our data do not provide a thorough treatise, there is a tangible link between Hg host phase and the depositional environment, with clay minerals as the dominant host of Hg in coastal environments (e.g., Wilson Lake, Ancora), and iron and manganese oxyhydroxides as likely important hosts of Hg in deep ocean environments (e.g., 30/14–1, Site 1262) (Gobeil and Cossa, 1993).

Correlation analysis provides an efficient and objective method of assessing Hg host phases, although it is not as thorough and direct as, for example, microprobe and scanning electron microscopy with energy-dispersive X-ray spectroscopy (e.g., Shen et al., 2019b, 2022a). One drawback of the correlation method we use is that Al content is not a perfect proxy for clay, and different clays have different affinities with Hg (Kongchum et al., 2011). Equally, TS contents in sedimentary rocks will typically represent a combination both sulfide and sulphate, and sulphate is unlikely to be a significant host of Hg. The type of organic matter also matters, as robust correlations between Hg and TOC arise mainly from soluble organic matter (Sanei and Goodarzi, 2006). Furthermore, correlation strength and significance can be related to the number of data, and/or analytical error. At the same time, correlations between Hg and TOC, TS, Al etc. can be strong if TOC, TS and Al are related, for example in anoxic settings where TOC will likely correlate strongly with TS (Shen et al., 2020), or where variable carbonate content strongly controls the abundance of other components via a dilution effect (as suggested above for Site 1262).

5.2. The temporal and spatial distribution of mercury enrichment across the PETM

Previous studies have demonstrated strong spatial variability in Hg enrichment across the PETM (Jones et al., 2019; Tremblin et al., 2022). Here, we capitalize on our larger compilation and use of a unified age model to assess Hg enrichment (Hg_{EF}) through time at all of the studied sites (Fig. 7). It is clear that there is no consistent pattern in Hg_{EF} across the PETM at the 19 studied sites (Fig. 7). For instance, some sites display significant increases in Hg_{EF} across the CIE onset (22/10a-4, E-8X), and some sites show significant increases in Hg_{EF} across the CIE body (BH09/2005, Esplugafreda). Other sites exhibit relatively constant Hg_{EF} across the CIE (ACEX, Bass River).

To help establish whether clear changes and patterns occur in Hg enrichment through the PETM, one-sided Wilcoxon rank sum tests are used to assess whether Hg_{EF} in each interval (CIE onset, body, recovery and post-CIE) is significantly higher than the pre-CIE interval (Fig. 8). This was done because we assume that the pre-CIE interval most likely reflects background conditions not significantly affected by volcanism. Although this assumption may be incorrect, it is valuable to understand how Hg_{EF} changed during the CIE in comparison to the pre-CIE interval for each site. A further caveat is that the change of Hg_{EF} at some sites across the carbon isotope-defined stages may be gradual. For example, Hg_{EF} values increased gradually prior to the onset of the CIE at sites 22/10a-4, E-8X, and BH09/2005. As a result, the CIE onset values are similar to the pre-CIE values. Equally, some sites are limited by a paucity of samples in the CIE onset, which spanned a relatively short duration (20 kyr as defined in this study). Carbonate dissolution and thus stratigraphic incompleteness during the CIE onset is also a known issue (Bralower et al., 2018). Thus, Hg_{EF} in the CIE onset interval may not be representative (e.g. Blake Nose). For intervals with few data it can be impossible to obtain robust p-values using Wilcoxon rank sum testing (e.g., ACEX, Esplugafreda, Bass River).

Ultimately, 5 out of 13 sites show significantly higher CIE onset Hg_{EF} values compared to the pre-CIE (22/10a-4, 30/14–1, E-8X, Ancora and Wilson Lake, Fig. 8). The other 6 sites in our compilation had one or no data points in the CIE onset interval, and therefore could not be tested (25/11–17, ACEX, Esplugafreda, Bass River, Millville, Blake Nose, Fig. 8). Eight out of 18 sites show significantly higher CIE body Hg_{EF} values compared to the pre-CIE (22/10a-4, 30/14–1, BH09/2005, Lussagnet, Esplugafreda, Ancora, Wilson Lake and Millville, Fig. 8). Only 4 sites out of 14 show significantly higher Hg_{EF} values in the CIE recovery relative to the pre-CIE interval (30/14–1, Lussagnet, Wilson Lake and Blake Nose), and 4 sites out of 14 show significantly higher Hg_{EF} values after the CIE compared to the pre-CIE (23/16b-9, 30/14–1 and Wilson Lake and Site 1262).

The 5 sites that show significantly increased Hg_{EF} values through the CIE onset are from the North Sea Basin (i.e., close to NAIP) and New Jersey coastal plain (Fig. 8). Six out of the remaining 14 quantifiable sites (25/11–17, 23/16b-9, BH09/2005, Lussagnet and Serraduy, Esplugafreda) also show higher Hg_{EF} through the CIE onset compared to the pre-CIE interval, but the difference is not statistically significant (Fig. 8). These sites are also reasonably close to NAIP (i.e., North Sea Basin, Arctic and the Pyrenean foreland basin; all within 4000 km of the NAIP). Sites that clearly show no increase in Hg_{EF} at the CIE onset include Blake Nose, Dababiya and Site 1262, which are relatively far from the NAIP. Taken together, the data support the inference of increased magmatic activity during the CIE onset relative to the pre-CIE interval, with this increase most likely to be significant within 4000 km of the NAIP.

5.3. Evaluating magmatism through the PETM based on compiled Hg_{EF} curves

To gain a high-resolution overview of the temporal evolution of Hg_{EF} through the PETM, Hg_{EF} values from the 19 studied sites are compiled together. To build this compilation, Hg_{EF} data for samples with <0.2% TOC were removed following Grasby et al. (2019) (see Section 2; Fig. 9). A total of 986 datapoints are plotted, yielding a composite record of age-calibrated Hg_{EF} across the PETM (Fig. 9F). To minimize bias and capture the pattern of relative changes in Hg_{EF}, the Hg_{EF} data at each of the 19

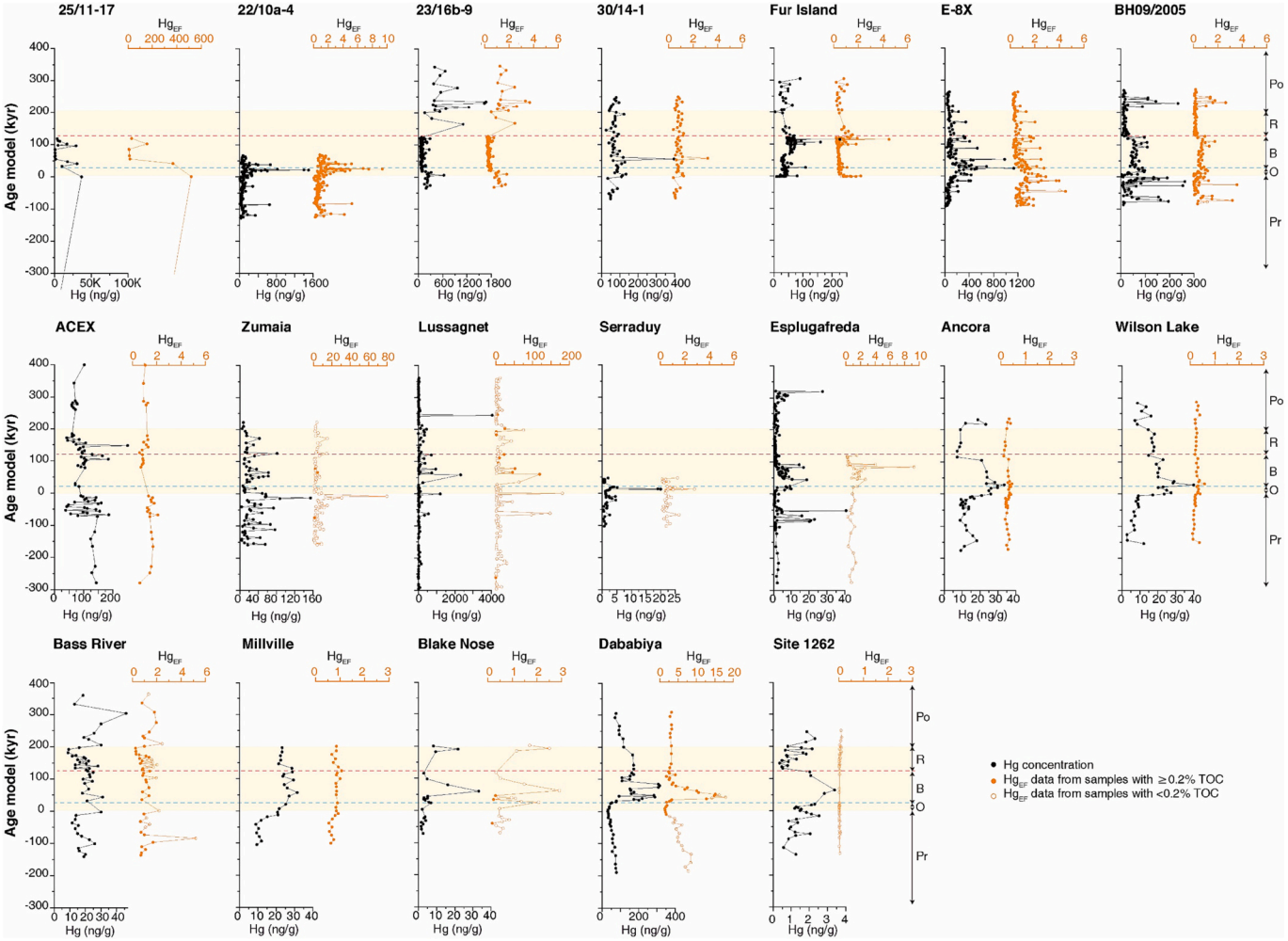

Fig. 7. Compilation of Hg and Hg_{EF} from all 19 studied sites plotted against age, and ordered by distance from the NAIP (i.e., 25/11–17 = closest, ODP Site 1262 = furthest). PETM CIE is highlighted with yellow shading. Pr = pre-CIE, O = CIE onset, B = CIE body, R = CIE recovery, Po = post-CIE. (For interpretation of the references to colour in this figure legend, the reader is referred to the web version of this article.)

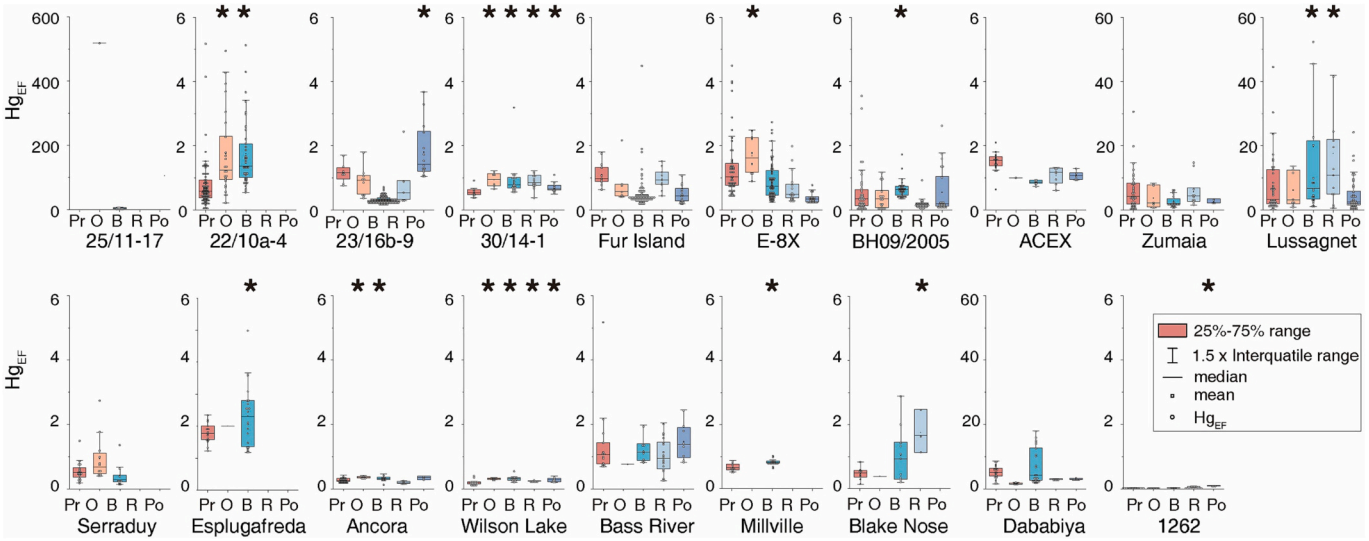

Fig. 8. Box and whisker plots of Hg_{EF} data from all 19 studied sites, with data at each site divided into pre-CIE (Pr), CIE onset (O), CIE body (B), CIE recovery (R), and post-CIE (Po) stages. Asterisks indicate that the median Hg_{EF} value for the corresponding stage is significantly higher than the median of the pre-onset Hg_{EF} value (at the 0.05 significance level), as determined by Wilcoxon rank sum tests. See main text for details.

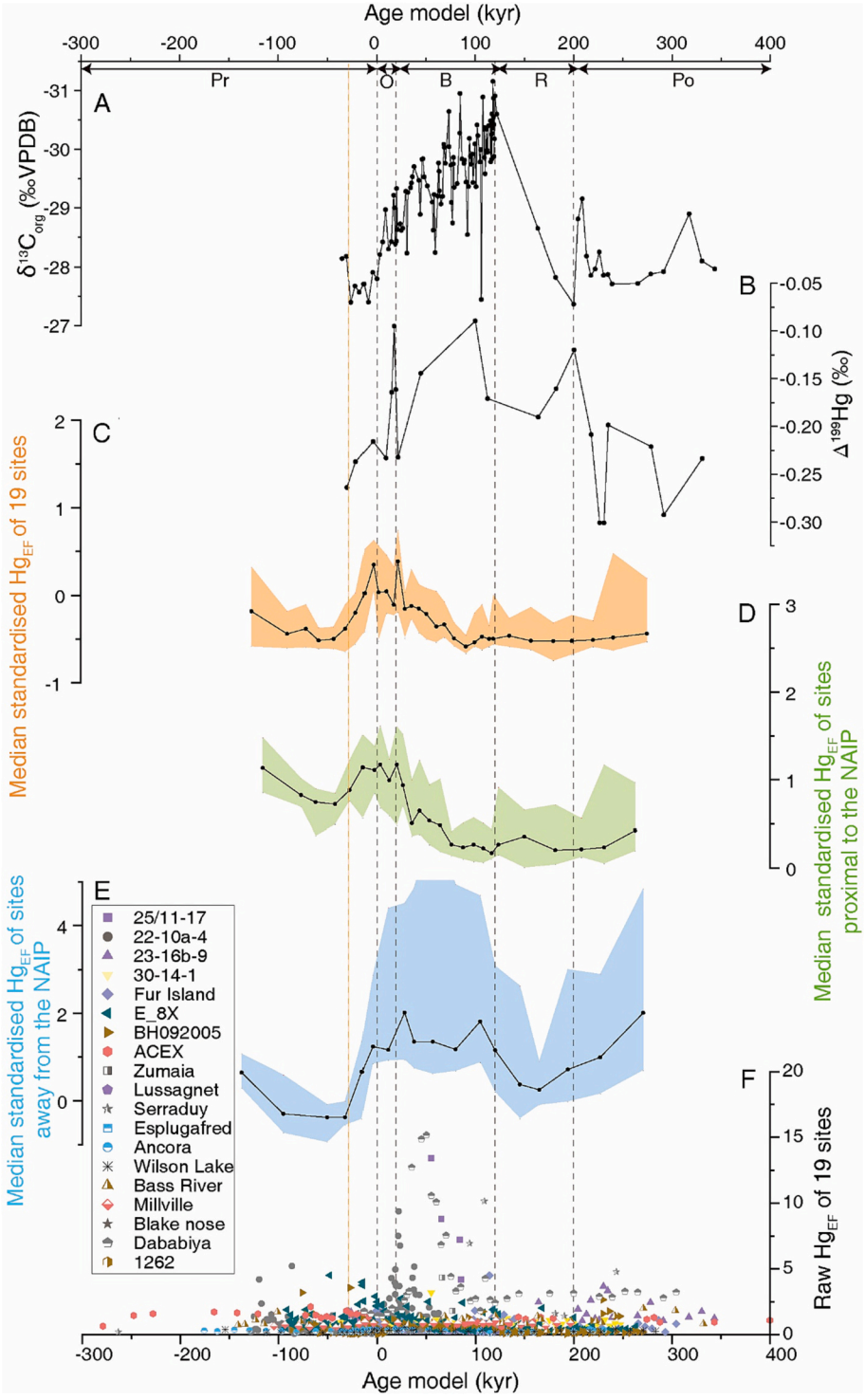

Fig. 9. Compiled temporal changes in Hg_{EF} across the PETM, with the $\delta^{13}C_{org}$ and $\Delta^{199}Hg$ from Well 23/16b-9 in the North Sea Basin also shown for reference. All data are plotted using the PETM age model of Westerhold et al. (2018) and Cui et al. (2011) (see main text for details). Hg_{EF} data from samples with <0.2% TOC are not used. See main text for details of PETM subdivisions. (A) Organic carbon-isotopes of Well 23/16b-9 ($\delta^{13}C_{org}$) (Jin et al., 2022). (B) $\Delta^{199}Hg$ from Well 23/16b-9 (Jin et al., 2023) (C) Median Hg_{EF} of all sites and the 95% confidence interval determined using bootstrapping. (D) Median Hg_{EF} of sites relatively proximal (<2500 km) to the NAIP (sites in the North Sea Basin, Spitsbergen, Arctic, France and Spain) and the 95% confidence interval determined using bootstrapping. (E) Median Hg_{EF} of sites relatively distal (>2500 km) from the NAIP (sites in New Jersey coastal plain, Atlantic and Egypt) and the 95% confidence interval determined using bootstrapping. See main text for details of median curve construction and bootstrapping. (F) Raw Hg_{EF} of the 19 sites, from 300 kyr before the CIE onset to 400 kyr after the CIE onset. 0 kyr marks the onset of the CIE. Dashed vertical orange line shows approximate timing of the increase in median Hg_{EF} in all curves, 30 kyr prior to the onset of the CIE. See main text for details. Pr = pre-CIE, O = CIE onset, B = CIE body, R = CIE recovery, Po = post-CIE.

sites were standardized to zero mean and a standard deviation of 1 (Fig. 9C). To investigate the effect of distance from the NAIP, the 19 sites were also split into 2 groups. Group one (Fig. 9D) includes sites relatively proximal to the NAIP (<2500 km, i.e., sites in the North Sea Basin, Spitsbergen, Arctic, France and Spain), and group two (Fig. 9E) contains sites distal to NAIP (>2500 km, i.e., sites in New Jersey coastal plain, North Atlantic, Egypt and Walvis Ridge). For these two groups, the raw Hg_{EF} data were standardized by dividing by the standard deviation, but the mean values were not subtracted (as done in Fig. 9C) in order to visualize differences in Hg_{EF} depending on distance from the NAIP (Figs. 9D and E). The median Hg_{EF} over time in Figs. 9C–E was calculated by binning the data into bins that each contain the same number of data points, and calculating the median for each bin). In Fig. 9C (all sites) and Fig. 9D (sites proximal to NAIP), each bin contains ~30 data points, and in Fig. 9E (sites distal to NAIP), each bin contains ~10 data points. In practice, this binning means that in time intervals with few data the bins span wider time intervals, and vice versa. Bootstrapping of data within each bin was employed to generate 95% confidence intervals for each calculated median value (shading in Figs, 9C-E).

Among the 19 sites, the majority of datapoints are from unweathered borehole samples and samples from 6 sites were from outcrops with Hg all mainly hosted by organic matter (Fur Island, Jones et al., 2019, 2023; Zumaia, Serraduy and Esplugafreda, Tremblin et al., 2022; Dababiya, Keller et al., 2018). At Fur Island, exposed unweathered sediments were sampled (Jones et al., 2019). At Dababiya, it is possible that relatively high Hg/TOC values (Keller et al., 2018) were caused at least in part by diagenesis and weathering processes (Jones et al., 2019), which could lead to loss of TOC relative to Hg and hence increase Hg/TOC (Charbonnier et al., 2020). Sample weathering information at Zumaia, Serraduy and Esplugafreda has not been published (Tremblin et al., 2022). At Serraduy and Esplugafreda, the influence of weathering may be low, and there are no extremely high Hg/TOC values that might indicate post-depositional alteration (e.g., Hg/TOC ratios >1000 ppb/wt%, Charbonnier et al., 2020). There are extremely high Hg/TOC ratios of up to 5740 ppb/wt% and 13,053 ppb/wt% in the Zumaia and Lussagnet cores, respectively. The majority of these high Hg/TOC samples from the Pyrenean foreland have <0.2% TOC and were therefore not used to build the median Hg_{EF} curves in Fig. 9.

Using median Hg_{EF} to make the curves helps to minimize the influence of any extreme Hg_{EF} values that might be attributable to post-depositional processes. For completeness, we also built Hg_{EF} median curves using all available data (i.e., including samples with <0.2% TOC (Fig. S1). This approach means that data from deep sea sections (where TOC is generally <0.2%) is better represented in the compilation. Both approaches yield similar curves (cf. Figs. 9 and S1). This suggests that low TOC data do not significantly influence the pattern of Hg_{EF} change through the PETM, but do make it somewhat noisier. One obvious drawback of our approach is that in time intervals with few data the median curve is of relatively low resolution (as partly reflected by large bootstrap errors). Another caveat is that sites with the most data points will have the biggest influence on the median curve.

As discussed in Section 3.3, Hg_{EF} is calculated by normalizing to an average expected Hg/host phase value (i.e., $Hg/host_{background}$). An alternative method to establish a non-volcanically influenced background composition of mercury (Hg) in a given PETM section involves assuming that there was negligible release of volcanic Hg 300 kyr prior to the PETM, and thus defining $Hg/host_{background}$ as the mean of the five lowest host-phase normalized Hg values in the pre-CIE interval of each record (e.g., Fig. S2). Both approaches yield similar curves (cf. Figs. 9 and S2), providing confidence that our methods provide a robust way of tracing trends in Hg enrichment through the PETM.

The median curve through the composite Hg_{EF} record of all 19 sites (Fig. 9C) is relatively stable up until 30.2 kyr before the CIE onset (mean = −0.41). An increase then occurs to a value of 0.35 at −2 kyr (actual bin width of −6 to 0 kyr for this median value). During the onset and early part of the CIE body (0 to 23 kyr), Hg_{EF} values remain relatively high (mean = 0.14) and then gradually decrease to relatively lower values during and after the latter part of the CIE body between 80 and 277 kyr (mean = −0.50).

The median Hg_{EF} profile for proximal sites (Fig. 9D) shows an increasing trend beginning at −42 kyr (i.e., before the CIE onset) and values remain relatively elevated from −14 to 20 kyr across the CIE onset (mean = 1.1) before decreasing. In contrast to Fig. 9C, median Hg_{EF} values for proximal sites between −116 kyr and − 42 kyr (mean = 0.86) are higher than the Hg_{EF} values during the CIE recovery and post-CIE (mean = 0.27 and 0.29, respectively).

For distal sites (Fig. 9E), the median Hg_{EF} curve shows relatively low Hg_{EF} values up to −32 kyr (mean = −0.10), and an increasing trend from −32 to 28 kyr across the pre-CIE and CIE onset intervals. Hg_{EF} values then begin to decrease at 105 kyr before increasing again at 165 kyr in the CIE recovery. Hg_{EF} values are higher during and after the CIE body but are likely not robust, as suggested by the wide 95% confidence interval determined by bootstrapping. The relatively high Hg_{EF} values from 194 to 271 kyr are biased by the high Hg_{EF} data from Bass River and Dababiya.

Prior to the CIE onset, the median Hg_{EF} curve for the proximal sites shows enrichment in Hg relative to the curve for the distal sites (Figs. 9D and E). This observation supports the idea that in the proximal sites prior to the PETM some Hg was derived from submarine volcanism and/or HTVCs with a limited dispersal range, and hence local NAIP magmatic activity was likely occurring in the late Paleocene well before (~120 kyr) the PETM.

All three composite records demonstrate a clear increase in Hg_{EF} beginning ~30 kyr before the CIE onset (Figs. 9C–E). This observation suggests a significant increase in magmatic activity just prior to the PETM. This finding aligns with geochronological data for the NAIP suggesting limited volcanic activity in the late Paleocene, increasing into the latest Paleocene (Wilkinson et al., 2017). Further support for volcanic activity immediately prior to the PETM comes from the presence of a negative shift in Os isotopes and an ash layer (SK1) just before the CIE onset at Fur Island (Jones et al., 2019, 2023). The negative shift in Os isotopes, as a tracer of globally averaged variations in the proportions of radiogenic versus unradiogenic Os, suggests an increased flux of unradiogenic Os from basalt weathering (Jones et al., 2023). At the same time, however, Os isotope data from ACEX and Tethys Ocean sites do not show a negative shift before the CIE onset (Dickson et al., 2015 and references therein). The absence of a negative shift in Os isotopes in the Tethys Ocean may be attributable to the limited preservation of pre-PETM strata at these localities, and it is possible that the Arctic was largely cut off from the global ocean in the case of the ACEX site (Jones et al., 2023). Recent work supports significant Hg release via thermogenic sources across the CIE onset, in addition to volcanic sources. Most pertinently, stable carbon isotope stratigraphy and high-resolution 3D seismic imaging provide compelling evidence that HTVCs on the mid-Norwegian margin formed just before the onset of the PETM and refilled during the onset and body of the CIE (Berndt et al., 2023), likely releasing substantial carbon and Hg at this time. Hg_{EF} in all 3 median curves reach a peak just prior to the start of the CIE (Figs. 9C–E). The elevated Hg_{EF} within the CIE onset itself, and the overall increase in Hg_{EF} from ~30 kyr prior to the CIE onset, is broadly consistent with the increasing $\Delta^{199}Hg$ values observed across this interval in Well 23/16b-9 (Jin et al., 2023; Fig. 9B).

Although an increase in volcanic and thermogenic Hg release can be inferred immediately before and throughout the CIE onset, our median curves show decreasing Hg_{EF} through the CIE body, suggesting decreasing Hg fluxes (Figs. 9C and D). This finding contradicts the 23/16b-9 $\Delta^{199}Hg$ record, which shows an increasing trend across the CIE body toward values of −0.09 ‰ (Fig. 9B), and has been interpreted as evidence that volcanic Hg fluxes were sustained and protracted (Jin et al., 2023). The contrasting relationship between Hg_{EF} and Hg isotopes here could potentially be due to Hg isotope data in Well 23/16b-9 being affected by a change in local Hg sources.

HTVCs are likely to emit highly variable amounts of Hg and the volatiles released may have a very limited distribution range (<20 km, Svensen et al., 2004, 2023). It has been proposed that multiple releases of thermogenic methane from hydrothermal vents were responsible for the long duration of the CIE body (Frieling et al., 2016). If the Hg released from such venting really did have a limited distribution as Svensen et al. (2023) suggest, then this hypothesis may be consistent with the decreasing Hg_{EF} trends observed through the CIE body (Figs. 9Cand D). The trend toward higher $\Delta^{199}Hg$ values during the CIE body in Well 23/16b-9, several hundred kilometers from known hydrothermal vents on the Norwegian shelf (Frieling et al., 2016), may indicate a protracted decline in terrestrial Hg fluxes relative to volcanic sources, rather than an increase in volcanic Hg fluxes. Alternatively, other volcanism besides hydrothermal venting may have operated at this time, but at an overall lower level than the pre-CIE volcanism (Jin et al., 2023). A shift in Hg sources further away from the 23/16b-9 site could also theoretically lead to an increase in $\Delta^{199}Hg$, because atmospheric photochemical reactions during transport can lead to higher $\Delta^{199}Hg$ (Shen et al., 2022b). This is perhaps unlikely, however, considering the relatively short distance between the 23/16b-9 site and the NAIP (~500 km). Overall, the declining Hg_{EF} during the CIE body may suggest an overall decrease in volcanism during the CIE body, though data on precise Hg emission rates and styles are currently lacking.

During the CIE recovery and post-CIE intervals, Hg_{EF} values remain consistently low, suggesting little global influx of volcanogenic Hg (Figs. 9C and D). As discussed in Section 5.2, only a handful of sites show significantly higher Hg_{EF} values during the CIE recovery or post-CIE interval compared to pre-CIE interval, and some of these data are likely not robust due to the limited amount of data (e.g., Blake Nose and Site 1262). Nevertheless, tephras commonly occur toward the end of the CIE body and in the post-CIE interval at Fur Island (Jones et al., 2019). In addition, the shift to more radiogenic Os isotope values at the very end of the CIE body at Fur Island may indicate at least in part waning volcanism (Jones et al., 2023). As noted by Larsen et al. (2003), ashes across the CIE onset and ashes from the end of the CIE body to post-CIE interval at Fur Island have heterogeneous compositions and were sourced from different volcanic centers within the NAIP (e.g., on the British Isles, East Greenland, and around the northeast Atlantic margin). The mineral assemblages are also different between the CIE onset ashes and the post CIE body ashes (Stokke et al., 2021). As such, it is possible that different volcanic source regions had different Hg fluxes, thus helping to account for changes in Hg_{EF} through the PETM.

5.4. Factors influencing Hg abundance through the PETM

5.4.1. Distance from the NAIP

Not all volcanic activity results in a disruption of the global Hg cycle (Percival et al., 2018), something perhaps evident in the compilation and alluded to in the discussion above. The impact of volcanism on Hg dispersal range depends on factors such as the specific style of volcanism (e.g., submarine versus subaerial) and eruption characteristics (height, volume, composition, duration, frequency) (Pyle and Mather, 2003; Percival et al., 2018). Explosive volcanism has the potential to cause global scale Hg disturbances due to the rapidity of atmospheric mixing relative to Hg residence time (0.5–1 year). The thickness of medium sand to clay-sized volcanic ash, which occurs in beds up to 8 cm thick in Fur Island during the CIE onset (700–1500 km from the NAIP), implies that plume heights were likely higher than 15 km (Stokke et al., 2020), likely indicating very wide dispersal.

Our compilation reveals a significant non-linear correlation between Hg content and distance from the NAIP during the CIE onset, with a Spearman correlation coefficient (ρ) of −0.763 (Fig. 10A, n = 18, *p*-value <0.001). Interestingly, however, there is no correlation between either normalized Hg (Hg/host phase) or Hg_{EF} with distance from the NAIP during the CIE onset (Figs. 10B and C). Indeed, the normalized Hg and Hg_{EF} values for all available sites are broadly comparable during the CIE onset (Figs. 10B and C).

The differing behaviors of Hg and normalized Hg in relation to distance from the NAIP suggest that the availability of Hg host phases in sedimentary environments plays a role in controlling the regional sequestration of Hg. For example, the deposition of tephra in areas proximal to volcanism can supply more nutrients to marine environments (Jones and Gislason, 2008; Olgun et al., 2013). The fertilizing effect of this ashfall could increase ocean productivity and lead to higher organic matter fluxes for areas closer to the NAIP, which may then lead to proportionally greater sequestration of Hg, whilst leaving Hg/TOC ratios relatively stable.

5.4.2. Water depth

As discussed above, the correlation between Hg abundance and distance from the NAIP is not a simple linear relationship, as each region exhibits a certain degree of heterogeneity (e.g., sites in the North Sea Basin and New Jersey coastal plain, Fig. 11). One plausible cause of this heterogeneity is the influence of water depth, which has the potential to modify Hg signals related to the distance from land (Them II et al., 2019; Yager et al., 2021). To investigate the impact of water depth on regional Hg distribution, sites were chosen that are far from the NAIP, thus largely avoiding the issue of NAIP distance affecting the results. Thus, the Hg data during the CIE onset from three New Jersey coastal plain sites and two Atlantic sites with well-constrained paleowater depth data were investigated (Fig. 12). The results show a significant correlation between water depth and Hg content during the CIE onset, but no correlation between water depth and normalized Hg or Hg_{EF}. This implies that water depth can affect the distribution of non-volcanogenic (i.e., terrestrial) Hg, which in the case of the New Jersey coastal plain sites is

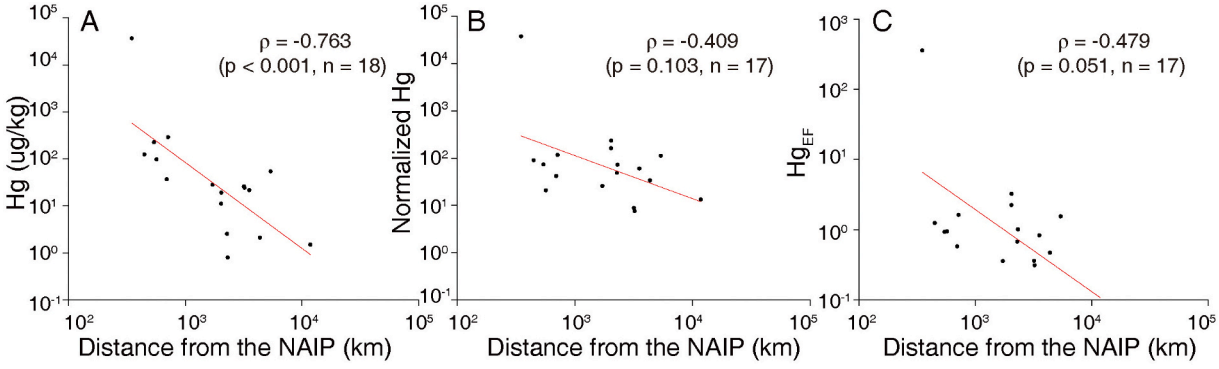

Fig. 10. Cross-plot showing influence of distance from NAIP on Hg content in the CIE onset interval. (A) Cross-plot of distance from NAIP versus median Hg content (B) Cross-plot of distance from NAIP versus median normalized Hg (i.e. Hg/host phase ratio). (C) Cross-plot of distance from NAIP versus median Hg_{EF} (Hg enrichment factor, see main text for details). Correlation coefficients are the Spearman ρ values. Note logarithmic axes.

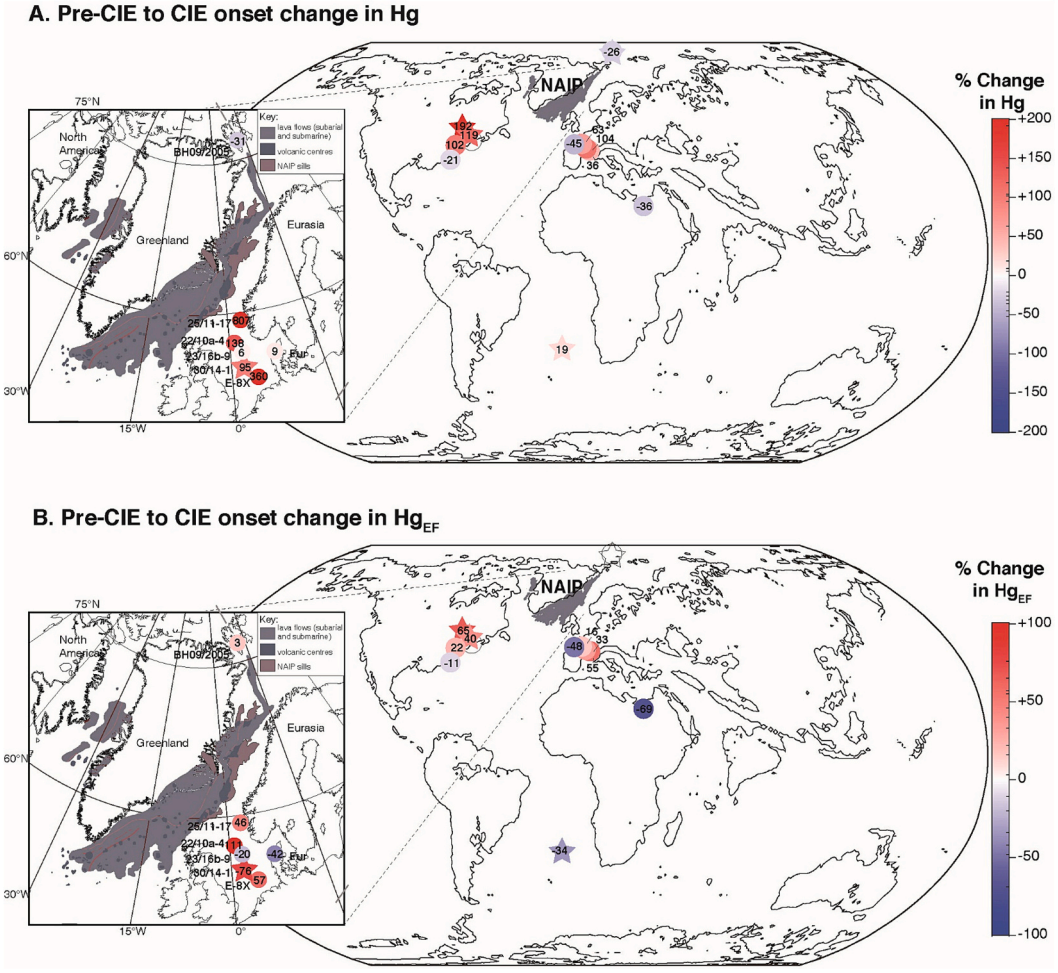

Fig. 11. Maps showing changes in Hg across the PETM onset. (A) Map showing the percent change in Hg content (ng/g) across the pre-CIE to CIE onset intervals. (B) Map showing the percent change in median Hg_{EF} across the pre-CIE to CIE onset intervals. Red colours indicate that Hg or Hg_{EF} in the CIE onset was higher than in the pre-CIE interval. Blue colours indicate the opposite. Map modified from Tierney et al. (2020). Inset map shows the location of the NAIP and sites close to the NAIP (modified from Jones et al. (2019) and Stokke et al. (2020). (For interpretation of the references to colour in this figure legend, the reader is referred to the web version of this article.)

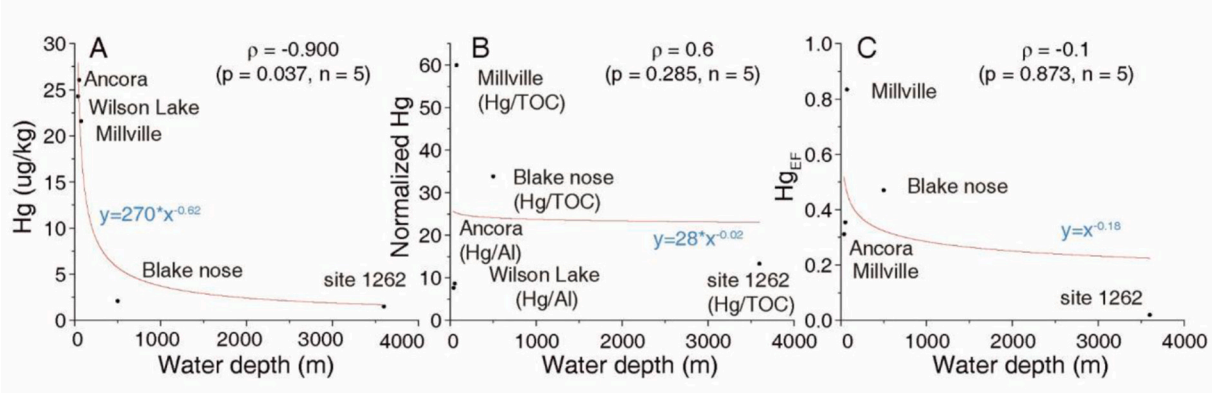

Fig. 12. Cross-plots showing the influence of water depth on Hg content in the CIE onset interval. (A) Cross-plot of water depth versus median Hg content. (B) Cross-plot of water depth versus median normalized Hg (i.e., Hg/host phase ratio). (C) Cross-plot of water depth versus median Hg_{EF}. Correlation coefficients are the Spearman ρ values. Note logarithmic axes.

likely derived from clay minerals in rivers that flow into the coastal ocean (Liu et al., 2021c). This result concurs with Them II et al. (2019) and Shen et al. (2020), who suggested that the concentration of terrestrial Hg varies with distance from river mouths. This may be a more plausible explanation than water depth-dependent organic matter degradation, as suggested by Yager et al. (2021). It is possible that other sites may also be influenced by water depth, but the effect is difficult to disentangle from the influence of NAIP distance, and because

paleowater depths are uncertain for many sites.

At a global scale, the correlation between water depth and Hg content during the onset is more complex. For example, significant differences in Hg abundance exist between deep sea sites of comparable depth (Well 22/10a-4 and Blake Nose). This suggests that Hg content at these sites was not predominantly influenced by the non-volcanogenic factor of water depth. Overall, the effect of water depth is perhaps less important than the effect of NAIP distance in controlling Hg enrichment during the PETM. A similar pattern of spatial distribution has been observed by Them II et al. (2019) during the Toarcian Oceanic Anoxic Event (T-OAE), which was associated with large-scale southern hemisphere volcanism. Them II et al. (2019) suggested that the proximity of landmasses to deposition sites affected both Hg and Hg/TOC during the T-OAE. In their work, they inferred that this dependency on geographic proximity to land implied that the primary source of Hg must have been terrestrial (Them II et al., 2019).

5.4.3. Sedimentation rates and organic matter burial rates

Changes in sedimentation rate have the potential to affect the concentration of Hg via dilution. For example, a decrease in sedimentation rate may result in higher atmospherically-sourced Hg concentration in a sediment, and an increased sedimentation rate could result in a lower atmospherically-sourced Hg concentration in a sediment, other things being equal. At the same time, however, the dilution effect linked to a change in clastic sediment flux could also reasonably lead to concomitant changes in marine organic matter and sulfide, leaving Hg/TOC and Hg/TS ratios unchanged. Nevertheless, if terrestrially-derived Hg and organic matter fluxes were significant (e.g. Them II et al., 2019) then changes in terrigenous sedimentation rate could indeed alter Hg/TOC ratios. To investigate this, we assessed the correlation between estimated sedimentation rates for each interval of the PETM (onset, body and recovery) at each of the 19 sites with the median values of Hg, TOC, Hg/TOC and Hg/host phase ratio for those intervals (Fig. S3). Results indicate that sedimentation rates do not correlate with Hg, TOC, Hg/TOC or Hg/host phase ratio (Fig. S3). Thus, in this study at least, sedimentation rate is unlikely to significantly influence calculated Hg_{EF}.

It is possible that a local excess supply of organic matter may result in lowered Hg/TOC ratios, and indeed there is evidence that organic matter burial increased dramatically during the PETM, especially in marginal seas (e.g., Kaya et al., 2022; Papadomanolaki et al., 2022). Nevertheless, among the 19 studied sites, only 2 sites showed a decrease in Hg/TOC that could conceivably have been caused by elevated TOC content (in the latter part of the CIE body at Fur Island and Dababiya), which is unlikely to significantly affect our compiled Hg_{EF} median curves (Figs. 9C–E).

6. Conclusions

We have compiled and analyzed Hg data from globally distributed PETM sites, allowing us to determine the spatial and temporal distribution of Hg across this event. Our results indicate that Hg enrichments (as quantified by Hg_{EF}) increased ~30 kyr prior to and within the onset of the PETM CIE, particularly at sites within 4000 km of the NAIP. This finding supports the view that large-scale NAIP volcanism and/or thermogenic degassing from contact metamorphism was active just prior to the PETM and plausibly triggered the event. The observed decline in Hg_{EF} during the CIE body ostensibly suggests waning magmatic activity, and this is perhaps supported by the absence of tephras around the NAIP area during this interval. However, Hg isotope and Os isotope data may indicate ongoing release of volcanic Hg through the CIE body. Generally low Hg_{EF} values are observed in the CIE recovery, despite some evidence for renewed volcanism (such as the reappearance of tephra deposits at Fur Island). Taken together, these apparent discrepancies likely underline how changing magmatic style plays an important role in controlling Hg emission fluxes and dispersion distances.

Although a clear signal of large-scale magmatism is apparent across the PETM onset, our work also highlights important caveats that need to be considered when using Hg as a proxy for paleo-volcanism, including water depth of the depositional site, distance from likely Hg sources, and changes in sedimentation rate and/or organic matter burial rates. Our analysis suggests that distance from the NAIP likely had a greater impact on Hg content than water depth.

CRediT authorship contribution statement

Simin Jin: Conceptualization, Methodology, Formal analysis, Investigation, Writing – original draft. **David B. Kemp:** Conceptualization, Supervision, Funding acquisition, Writing – review & editing. **Jun Shen:** Investigation, Writing – review & editing. **Runsheng Yin:** Investigation, Writing – review & editing. **David W. Jolley:** Writing – review & editing. **Manuel Vieira:** Writing – review & editing. **Chunju Huang:** Supervision, Funding acquisition, Writing – review & editing.

Declaration of Competing Interest

The authors declare that they have no known competing financial interests or personal relationships that could have appeared to influence the work reported in this paper.

Data availability

Data will be made available on request.

Acknowledgments

We thank the International Ocean Discovery Program (IODP) and British Geological Survey for providing us with samples. We thank Shell UK and partners for their support and permission to publish this research. This work was supported by the National Natural Science Foundation of China (Grant Nos. 42230208, 42272033, 41888101, 42172039), the National Key R&D Program of China (2022YFF0803100; 2022YFF0802900). This work is a contribution to IGCP739.

Appendix A. Supplementary data

Supplementary data to this article can be found online at https://doi.org/10.1016/j.earscirev.2023.104647.

References

Bagnato, E., Aiuppa, A., Parello, F., Calabrese, S., D'alessandro, W., Mather, T.A., McGonigle, A.J.S., Pyle, D.M., Wängberg, I., 2007. Degassing of gaseous (elemental and reactive) and particulate mercury from Mount Etna volcano (Southern Italy). Atmos. Environ. 41 (35), 7377–7388.

Berndt, C., Planke, S., Alvarez Zarikian, Frieling, J., Jones, M.T., Millett, J.M., Yager, S. L., 2023. Shallow-water hydrothermal venting linked to the Palaeocene–Eocene Thermal Maximum. Nat. Geosci. 16 (9), 803–809.

Bøggild, O.B., 1918. Den vulkanske Aske i Moleret samt en Oversigt over Danmarks ældre Tertiærbjergarter. Bull. Geol. Soc. Den. 33, 1–159.

Boszke, L., Kowalski, A., Glosifiska, G., Szarek, R., Siepak, J., 2003. Environmental factors affecting speciation of mercury in the bottom sediments; an overview. Pol. J. Environ. Stud. 12 (1).

Bralower, T.J., Kump, L.R., Self-Trail, J.M., Robinson, M.M., Lyons, S., Babila, T., Ballaron, E., Freeman, K.H., Hajek, E., Rush, W., Zachos, J.C., 2018. Evidence for shelf acidification during the onset of the Paleocene-Eocene thermal maximum. Paleoceanogr. Paleoclimatol. 33 (12), 1408–1426.

Charbonnier, G., Adatte, T., Föllmi, K.B., Suan, G., 2020. Effect of intense weathering and postdepositional degradation of organic matter on Hg/TOC proxy in organic-rich sediments and its implicationsfor deep-time investigations. Geochem. Geophys. Geosyst. 21 (2) e2019GC008707.

Cui, Y., Kump, L.R., Ridgwell, A.J., Charles, A.J., Junium, C.K., Diefendorf, A.F., Freeman, K.H., Urban, N.M., Harding, I.C., 2011. Slow release of fossil carbon during the Palaeocene–Eocene Thermal Maximum. Nat. Geosci. 4 (7), 481–485.

DeConto, R.M., Galeotti, S., Pagani, M., Tracy, D., Schaefer, K., Zhang, T., Pollard, D., Beerling, D.J., 2012. Past extreme warming events linked to massive carbon release from thawing permafrost. Nature 484 (7392), 87–91.

Demers, J.D., Blum, J.D., Zak, D.R., 2013. Mercury isotopes in a forested ecosystem: implications for air-surface exchange dynamics and the global mercury cycle. Glob. Biogeochem. Cycles 27 (1), 222–238.
Dickens, G.R., O'Neil, J.R., Rea, D.K., Owen, R.M., 1995. Dissociation of oceanic methane hydrate as a cause of the carbon isotope excursion at the end of the Paleocene. Paleoceanography 10 (6), 965–971.
Dickson, A.J., Cohen, A.S., Coe, A.L., Davies, M., Shcherbinina, E.A., Gavrilov, Y.O., 2015. Evidence for weathering and volcanism during the PETM from Arctic Ocean and Peri-Tethys osmium isotope records. Palaeogeogr. Palaeoclimatol. Palaeoecol. 438, 300–307.
Emili, A., Koron, N., Covelli, S., Faganeli, J., Acquavita, A., Predonzani, S., De Vittor, C., 2011. Does anoxia affect mercury cycling at the sediment–water interface in the Gulf of Trieste (northern Adriatic Sea)? Incubation experiments using benthic flux chambers. Appl. Geochem. 26 (2), 194–204.
Farrah, H., Pickering, W.F., 1978. The sorption of mercury species by clay minerals. Water Air Soil Pollut. 9 (1), 23–31.
Frieling, J., Svensen, H.H., Planke, S., Cramwinckel, M.J., Selnes, H., Sluijs, A., 2016. Thermogenic methane release as a cause for the long duration of the PETM. Proc. Natl. Acad. Sci. 113 (43), 12059–12064.
Frieling, J., Mather, T.A., März, C., Jenkyns, H.C., Hennekam, R., Reichart, G.-J., Slomp, C.P., van Helmond, N.A.G.M., 2023. Effects of redox variability and early diagenesis on marine sedimentary Hg records. Geochim. Cosmochim. Acta 351, 78–95.
Gobeil, C., Cossa, D., 1993. Mercury in sediments and sediment pore water in the Laurentian Trough. Can. J. Fish. Aquat. Sci. 50 (8), 1794–1800.
Grasby, S.E., Sanei, H., Beauchamp, B., Chen, Z., 2013. Mercury deposition through the Permo–Triassic biotic crisis. Chem. Geol. 351, 209–216.
Grasby, S.E., Beauchamp, B., Bond, D.P., Wignall, P.B., Sanei, H., 2016. Mercury anomalies associated with three extinction events (Capitanian crisis, latest Permian extinction and the Smithian/Spathian extinction) in NW Pangea. Geol. Mag. 153 (2), 285–297.
Grasby, S.E., Them II, T.R., Chen, Z., Yin, R., Ardakani, O.H., 2019. Mercury as a proxy for volcanic emissions in the geologic record. Earth Sci. Rev. 196, 102880.
Gutjahr, M., Ridgwell, A., Sexton, P.F., Anagnostou, E., Pearson, P.N., Pälike, H., Norris, R.D., Foster, G.L., 2017. Very large release of mostly volcanic carbon during the Palaeocene-Eocene Thermal Maximum. Nature 548 (7669), 573–577.
Horowitz, A.J., 1991. A Primer on Sediment-Trace Element Chemistry, vol. 2. Lewis Publishers, Chelsea.
Hu, D., Li, M., Chen, J., Luo, Q., Grasby, S.E., Zhang, T., Yuan, S., Xu, Y., Finney, S.C., Sun, L., Shen, Y., 2021. Major volcanic eruptions linked to the Late Ordovician mass extinction: evidence from mercury enrichment and Hg isotopes. Glob. Planet. Chang. 196, 103374.
Jin, S., Kemp, D.B., Jolley, D.W., Vieira, M., Zachos, J.C., Huang, C., Li, M., Chen, W., 2022. Large-scale, astronomically paced sediment input to the North Sea Basin during the Paleocene Eocene thermal Maximum. Earth Planet. Sci. Lett. 579, 117340.
Jin, S., Kemp, D.B., Yin, R., Sun, R., Shen, J., Jolley, D.W., Vieira, M., Huang, C., 2023. Mercury isotope evidence for protracted North Atlantic magmatism during the Paleocene-Eocene thermal Maximum. Earth Planet. Sci. Lett. 602, 117926.
Jolley, D.W., Millett, J.M., Schofield, N., Broadley, L., 2021. Stratigraphy of volcanic rock successions of the North Atlantic rifted margin: the offshore record of the Faroe–Shetland and Rockall basins. Earth Environ. Sci. Trans. R. Soc. Edinb. 112 (2), 61–88.
Jones, M.T., Gislason, S.R., 2008. Rapid releases of metal salts and nutrients following the deposition of volcanic ash into aqueous environments. Geochim. Cosmochim. Acta 72 (15), 3661–3680.
Jones, M.T., Percival, L.M., Stokke, E.W., Frieling, J., Mather, T.A., Riber, L., Schubert, B. A., Schultz, B., Tegner, C., Planke, S., Svensen, H.H., 2019. Mercury anomalies across the Palaeocene–Eocene thermal maximum. Clim. Past 15 (1), 217–236.
Jones, M.T., Stokke, E.W., Rooney, A.D., Frieling, J., Pogge von Strandmann, P.A., Wilson, D.J., Svensen, H.H., Planke, S., Adatte, T., Thibault, N.R., Vickers, M.L., 2023. Tracing North Atlantic volcanism and seaway connectivity across the Paleocene–Eocene Thermal Maximum (PETM). EGUsphere, pp. 1–53.
Kaya, M.Y., Dupont-Nivet, G., Frieling, J., Fioroni, C., Rohrmann, A., Altıner, S.Ö., Zhaojie, G., 2022. The Eurasian epicontinental sea was an important carbon sink during the Palaeocene-Eocene thermal maximum. Commun. Earth Environ. 3 (1), 124.
Keller, G., Mateo, P., Punekar, J., Khozyem, H., Gertsch, B., Spangenberg, J., Bitchong, A. M., Adatte, T., 2018. Environmental changes during the Cretaceous-Paleogene mass extinction and Paleocene-Eocene thermal maximum: implications for the Anthropocene. Gondwana Res. 56, 69–89.
Kender, S., Bogus, K., Pedersen, G.K., Dybkjær, K., Mather, T.A., Mariani, E., Ridgwell, A., Riding, J.B., Wagner, T., Hesselbo, S.P., Leng, M.J., 2021. Paleocene/Eocene carbon feedbacks triggered by volcanic activity. Nat. Commun. 12, 5186.
Kongchum, M., Hudnall, W.H., Delaune, R.D., 2011. Relationship between sediment clay minerals and total mercury. J. Environ. Sci. Health A 46 (5), 534–539.
Larsen, L.M., Fitton, J.G., Pedersen, A.K., 2003. Paleogene volcanic ash layers in the Danish Basin: compositions and source areas in the North Atlantic Igneous Province. Lithos 71 (1), 47–80.
Liu, Z., Horton, D.E., Tabor, C., Sageman, B.B., Percival, L.M., Gill, B.C., Selby, D., 2019. Assessing the contributions of comet impact and volcanism toward the climate perturbations of the Paleocene-Eocene thermal maximum. Geophys. Res. Lett. 46 (24), 14798–14806.
Liu, X., Wang, Q., Peng, Y., Yin, R., Ma, Y., Zhao, L., Zhang, S., 2023. Intensified and apace bauxitization over the paleo-karstic surface linked to volcanism. Bulletin 135 (5–6), 1187–1205.
Liu, Z.R.R., Zhou, M.F., Wang, W., 2021a. Mercury anomalies across the Ediacaran–Cambrian boundary: evidence for a causal link between continental erosion and biological evolution. Geochim. Cosmochim. Acta 304, 327–346.
Liu, M., Zhang, Q., Maavara, T., Liu, S., Wang, X., Raymond, P.A., 2021c. Rivers as the largest source of mercury to coastal oceans worldwide. Nat. Geosci. 14 (9), 672–677.
Liu, Z.R.R., Zhou, M.F., Chen, W.T., Williams-Jones, A.E., Li, X.D., Yin, R.S., O'Brien, H., Lahaye, Y., 2021b. Mercury and sulfur isotopic evidence for the linkages between the ca. 510 Ma Kalkarindji large igneous province and trilobite crisis. Earth Planet. Sci. Lett. 566, 116947.
Makarova, M., Wright, J.D., Miller, K.G., Babila, T.L., Rosenthal, Y., Park, J.I., 2017. Hydrographic and ecologic implications of foraminiferal stable isotopic response across the US mid-Atlantic continental shelf during the Paleocene-Eocene Thermal Maximum. Paleoceanography 32 (1), 56–73.
McInerney, F.A., Wing, S.L., 2011. The Paleocene-Eocene Thermal Maximum: a perturbation of carbon cycle, climate, and biosphere with implications for the future. Annu. Rev. Earth Planet. Sci. 39, 489–516.
Olgun, N., Duggen, S., Andronico, D., Kutterolf, S., Croot, P.L., Giammanco, S., Censi, P., Randazzo, L., 2013. Possible impacts of volcanic ash emissions of Mount Etna on the primary productivity in the oligotrophic Mediterranean Sea: results from nutrient-release experiments in seawater. Mar. Chem. 152, 32–42.
Papadomanolaki, N.M., Sluijs, A., Slomp, C.P., 2022. Eutrophication and deoxygenation forcing of marginal marine organic carbon burial during the PETM. Paleoceanogr. Paleoclimatol. 37 (3) e2021PA004232.
Park, J., Stein, H.J., Georgiev, S.V., Hannah, J.L., 2022. Degradation of Hg signals on incipient weathering: Core versus outcrop geochemistry of Upper Permian shales, East Greenland and Mid-Norwegian Shelf. Chem. Geol. 608, 121030.
Percival, L.M.E., Jenkyns, H.C., Mather, T.A., Dickson, A.J., Batenburg, S.J., Ruhl, M., Hesselbo, S.P., Barclay, R., Jarvis, I., Robinson, S.A., Woelders, L., 2018. Does large igneous province volcanism always perturb the mercury cycle? Comparing the records of Oceanic Anoxic Event 2 and the end-Cretaceous to other Mesozoic events. Am. J. Sci. 318 (8), 799–860.
Pyle, D.M., Mather, T.A., 2003. The importance of volcanic emissions for the global atmospheric mercury cycle. Atmos. Environ. 37 (36), 5115–5124.
Qiu, Z., Wei, H., Tian, L., Corso, J.D., Zhang, J., Zou, C., 2022. Different controls on the Hg spikes linked the two pulses of the Late Ordovician mass extinction in South China. Sci. Rep. 12 (1), 5195.
Rakociński, M., Książak, D., Pisarzowska, A., Marynowski, L., 2022. Mercury evidence of intense submarine volcanism and hydrothermal activity during a mid-Tournaisian anoxic event in the Carnic Alps. Gondwana Res. 109, 225–238.
Ravichandran, M., 2004. Interactions between mercury and dissolved organic matter—a review. Chemosphere 55 (3), 319–331.
Saker-Clark, M., Kemp, D.B., Coe, A.L., 2019. Portable X-ray fluorescence spectroscopy as a tool for cyclostratigraphy. Geochem. Geophys. Geosyst. 20 (5), 2531–2541.
Sanei, H., Goodarzi, F., 2006. Relationship between organic matter and mercury in recent lake sediment: the physical–geochemical aspects. Appl. Geochem. 21 (11), 1900–1912.
Saunders, A.D., Fitton, J.G., Kerr, A.C., Norry, M.J., Kent, R.W., 1997. The north Atlantic igneous province. In: Mahoney, J.J., Coffin, M.F. (Eds.), Large Igneous Provinces. American Geophysical Union, Geophysical Monograph, 100, pp. 45–93.
Scaife, J.D., Ruhl, M., Dickson, A.J., Mather, T.A., Jenkyns, H.C., Percival, L.M.E., Hesselbo, S.P., Cartwright, J., Eldrett, J.S., Bergman, S.C., Minisini, D., 2017. Sedimentary mercury enrichments as a marker for submarine large igneous province volcanism? Evidence from the Mid-Cenomanian event and Oceanic Anoxic Event 2 (Late cretaceous). Geochem. Geophys. Geosyst. 18 (12), 4253–4275.
Schmitz, B., Peucker-Ehrenbrink, B., Heilmann-Clausen, C., Åberg, G., Asaro, F., Lee, C.T. A., 2004. Basaltic explosive volcanism, but no comet impact, at the Paleocene–Eocene boundary: high-resolution chemical and isotopic records from Egypt, Spain and Denmark. Earth Planet. Sci. Lett. 225 (1–2), 1–17.
Schroeder, W.H., Munthe, J., 1998. Atmospheric mercury—an overview. Atmos. Environ. 32 (5), 809–822.
Selin, N.E., 2009. Global biogeochemical cycling of mercury: a review. Annu. Rev. Environ. Resour. 34, 43–63.
Shen, J., Chen, J., Algeo, T.J., Yuan, S., Feng, Q., Yu, J., Zhou, L., O'Connell, B., Planavsky, N.J., 2019a. Evidence for a prolonged Permian-Triassic extinction interval from global marine mercury records. Nat. Commun. 10, 1563.
Selin, N.E., Jacob, D.J., Yantosca, R.M., Strode, S., Jaegle, L., Sunderland, E.M., 2008. Global 3-D land-ocean-atmosphere model for mercury: Present-day versus preindustrial cycles and anthropogenic enrichment factors for deposition. Glob. Biogeochem. Cycles. 22 (2).
Shen, J., Algeo, T.J., Chen, J., Planavsky, N.J., Feng, Q.L., Yu, J.X., Liu, J.L., 2019b. Mercury in marine Ordovician/Silurian boundary sections of South China is sulfide hosted and non-volcanic in origin. Earth Planet. Sci. Lett. 511, 130–140.
Shen, J., Algeo, T.J., Planavsky, N.J., Yu, J., Feng, Q., Song, H., Chen, J., 2019d. Mercury enrichments provide evidence of Early Triassic volcanism following the end-Permian mass extinction. Earth-Science Reviews 195, 191–212.
Shen, J., Algeo, T.J., Planavsky, N.J., Yu, J., Feng, Q., Song, H., Song, H., Rowe, H., Zhou, L., Chen, J., 2019c. Mercury enrichments provide evidence of Early Triassic volcanism following the end-Permian mass extinction. Earth Sci. Rev. 195, 191–212.
Shen, J., Feng, Q., Algeo, T.J., Liu, J., Zhou, C., Wei, W., Liu, J., Them II, T.R., Gill, B.C., Chen, J., 2020. Sedimentary host phases of mercury (Hg) and implications for use of Hg as a volcanic proxy. Earth Planet. Sci. Lett. 543, 116333.
Shen, J.*., Yin, R., Zhang, S., Algeo, T.J., Bottjer, D.J., Yu, J.X., Xu, G.Z., Penman, D., Wang, Y.D., Li, L.Q., Shi, X., Planavsky, N.J., Feng, Q.L., Xie, S.C., 2022a. Intensified continental chemical weathering and carbon-cycle perturbations linked to volcanism during the Triassic–Jurassic transition. Nat. Commun. 13, 299.

Shen, J., Algeo, T.J., Feng, Q., 2022b. Mercury isotope evidence for a non-volcanic origin of Hg spikes at the Ordovician-Silurian boundary, South China. Earth Planet. Sci. Lett. 594, 117705.
Shen, J., Chen, J., Yu, J., Algeo, T.J., Smith, R.M., Botha, J., Frank, T.D., Fielding, C.R., Ward, P.D., Mather, T.A., 2023. Mercury evidence from southern Pangea terrestrial sections for end-Permian global volcanic effects. Nat. Commun. 14 (1), 6.
Sial, A.N., Chen, J., Korte, C., Pandit, M.K., Spangenberg, J.E., Silva-Tamayo, J.C., de Lacerda, L.D., Ferreira, V.P., Barbosa, J.A., Gaucher, C., Pereira, N.S., Riedel, P.R., 2021. Hg isotopes and enhanced hg concentration in the meishan and guryul ravine successions: proxies for volcanism across the permian-triassic boundary. Front. Earth Sci. 9, 651224.
Sluijs, A., Schouten, S., Pagani, M., Woltering, M., Brinkhuis, H., Damsté, J.S.S., Dickens, G.R., Huber, M., Reichart, G.J., Stein, R., Matthiessen, J., 2006. Subtropical Arctic Ocean temperatures during the Palaeocene/Eocene thermal maximum. Nature 441 (7093), 610–613.
Sluijs, A., Brinkhuis, H., Schouten, S., Bohaty, S.M., John, C.M., Zachos, J.C., Reichart, G., Sinninghe Damste, J.S., Crouch, E.M., Dickens, G.R., 2007. Environmental pre-cursors to rapid light carbon injection at the Palaeocene/Eocene boundary. Nature 450 (7173), 1218–1221.
Stassen, P., Thomas, E., Speijer, R.P., 2012. Integrated stratigraphy of the Paleocene-Eocene thermal maximum in the New Jersey Coastal Plain: toward understanding the effects of global warming in a shelf environment. Paleoceanography 27 (4).
Stokke, E.W., Liu, E., Jones, M.T., 2020. Evidence of explosive hydromagmatic eruptions during the emplacement of the North Atlantic Igneous Province. Volcanica 3 (2), 227–250.
Stokke, E.W., Jones, M.T., Riber, L., Haflidason, H., Midtkandal, I., Schultz, B.P., Svensen, H.H., 2021. Rapid and sustained environmental responses to global warming: the Paleocene–Eocene Thermal Maximum in the eastern North Sea. Clim. Past 17 (5), 1989–2013.
Storey, M., Duncan, R.A., Tegner, C., 2007. Timing and duration of volcanism in the North Atlantic Igneous Province: implications for geodynamics and links to the Iceland hotspot. Chem. Geol. 241 (3–4), 264–281.
Svensen, H., Planke, S., Malthe-Sørenssen, A., Jamtveit, B., Myklebust, R., Rasmussen Eidem, T., Rey, S.S., 2004. Release of methane from a volcanic basin as a mechanism for initial Eocene global warming. Nature 429 (6991), 542–545.
Svensen, H.H., Jones, M.T., Percival, L.M., Grasby, S.E., Mather, T.A., 2023. Release of mercury during contact metamorphism of shale: Implications for understanding the impacts of large igneous province volcanism. Earth Planet. Sci. Lett. 619, 118306.
Svensen, H., Planke, S., Corfu, F., 2010. Zircon dating ties NE Atlantic sill emplacement to initial Eocene global warming. J. Geol. Soc. Lond. 167 (3), 433–436.
Tang, D., Fu, X., Shi, X., Zhou, L., Zheng, W., Li, C., Xu, D., Zhou, X., Xie, B., Zhu, X., Jiang, G., 2022. Enhanced weathering triggered the transient oxygenation event at~ 1.57 Ga. Geophys. Res. Lett. 49 (15) e2022GL099018.
Tessier, A.N.D.R.E., Campbell, P.G., Bisson, M.A.R.C., 1982. Particulate trace metal speciation in stream sediments and relationships with grain size: implications for geochemical exploration. J. Geochem. Explor. 16 (2), 77–104.
Them II, T.R., Jagoe, C.H., Caruthers, A.H., Gill, B.C., Grasby, S.E., Gröcke, D.R., Yin, R., Owens, J.D., 2019. Terrestrial sources as the primary delivery mechanism of mercury to the oceans across the Toarcian Oceanic Anoxic Event (Early Jurassic). Earth Planet. Sci. Lett. 507, 62–72.
Tierney, J.E., Poulsen, C.J., Montañez, I.P., Bhattacharya, T., Feng, R., Ford, H.L., Hönisch, B., Inglis, G.N., Petersen, S.V., Sagoo, N., Tabor, C.R., 2020. Past climates inform our future. Science 370 (6517), eaay3701.
Tomiyasu, T., Eguchi, T., Yamamoto, M., Anazawa, K., Sakamoto, H., Ando, T., Nedachi, M., Marumo, K., 2007. Influence of submarine fumaroles on the distribution of mercury in the sediment of Kagoshima Bay, Japan. Mar. Chem. 107, 173–183.
Tremblin, M., Khozyem, H., Adatte, T., Spangenberg, J.E., Fillon, C., Grauls, A., Hunger, T., Nowak, A., Läuchli, C., Lasseur, E., Roig, J.Y., Serrano, O., Calassou, S., Guillocheau, F., Castelltort, S., 2022. Mercury enrichments of the Pyrenean foreland basins sediments support enhanced volcanism during the Paleocene-Eocene thermal maximum (PETM). Glob. Planet. Chang. 212, 103794.
Wang, Y., Tan, J., Wang, W., Zhou, L., Tang, P., Kang, X., Dick, J., 2023. The influence of Late Ordovician volcanism on the marine environment based on high-resolution mercury data from South China. Bulletin 135 (3–4), 787–798.
Westerhold, T., Röhl, U., Wilkens, R.H., Gingerich, P.D., Clyde, W.C., Wing, S.L., Bowen, G.J., Kraus, M.J., 2018. Synchronizing early Eocene deep-sea and continental records–cyclostratigraphic age models for the Bighorn Basin Coring Project drill cores. Clim. Past 14 (3), 303–319.
Wieczorek, R., Fantle, M.S., Kump, L.R., Ravizza, G., 2013. Geochemical evidence for volcanic activity prior to and enhanced terrestrial weathering during the Paleocene Eocene Thermal Maximum. Geochim. Cosmochim. Acta 119, 391–410.
Wilkinson, C.M., Ganerød, M., Hendriks, B.W., Eide, E.A., 2017. Compilation and appraisal of geochronological data from the North Atlantic Igneous Province (NAIP). Geol. Soc. Lond. Spec. Publ. 447 (1), 69–103.
Wright, J.D., Schaller, M.F., 2013. Evidence for a rapid release of carbon at the Paleocene-Eocene thermal maximum. Proc. Natl. Acad. Sci. 110 (40), 15908–15913.
Wu, Y., Yin, R., Li, C., Chen, D., Grasby, S.E., Li, T., Ji, S., Tian, H., 2022. Global Hg cycle over Ediacaran–Cambrian transition and its implications for environmental and biological evolution. Earth Planet. Sci. Lett. 587, 117551.
Yager, J.A., West, A.J., Thibodeau, A.M., Corsetti, F.A., Rigo, M., Berelson, W.M., Bottjer, D.J., Greene, S.E., Ibarra, Y., Jadoul, F., Ritterbush, K.A., 2021. Mercury contents and isotope ratios from diverse depositional environments across the Triassic–Jurassic Boundary: towards a more robust mercury proxy for large igneous province magmatism. Earth Sci. Rev. 223, 103775.
Zachos, J.C., McCarren, H., Murphy, B., Röhl, U., Westerhold, T., 2010. Tempo and scale of late Paleocene and early Eocene carbon isotope cycles: Implications for the origin of hyperthermals. Earth Planet. Sci. Lett. 299 (1–2), 242–249.
Zachos, J.C., Röhl, U., Schellenberg, S.A., Sluijs, A., Hodell, D.A., Kelly, D.C., Thomas, E., Nicolo, M., Raffi, I., Lourens, L.J., McCarren, H., 2005. Rapid acidification of the ocean during the Paleocene-Eocene thermal maximum. Science 308 (5728), 1611–1615.
Zan, B., Mou, C., Lash, G.G., Ge, X., Wang, X., Wang, Q., Yan, J., Chen, F., Jin, B., 2021. An integrated study of the petrographic and geochemical characteristics of organic-rich deposits of the Wufeng and Longmaxi formations, western Hubei Province, South China: insights into the co-evolution of paleoenvironment and organic matter accumulation. Mar. Pet. Geol. 132, 105193.
Zhao, H., Shen, J., Algeo, T.J., Racki, G., Chen, J., Huang, C., Song, J., Qie, W., Gong, Y., 2022a. Mercury isotope evidence for regional volcanism during the Frasnian-Famennian transition. Earth Planet. Sci. Lett. 581, 117412.
Zhao, H., Grasby, S.E., Wang, X., Zhang, L., Liu, Y., Chen, Z.Q., Hu, Z., Huang, Y., 2022b. Mercury enrichments during the Carnian Pluvial Event (Late Triassic) in South China. GSA Bull. 134 (9–10), 2709–2720.